An Isogeometric analysis based method for frictional elastic contact problems with randomly rough surfaces

Han Hu[a,b], Anas Batou[b,*], Huajiang Ouyang[a]

[a] *Department of Mechanical, Materials and Aerospace Engineering, School of Engineering, University of Liverpool, Liverpool L69 7ZF, United Kingdom*
[b] *MSME, Univ Gustave Eiffel, CNRS UMR 8208, Univ Paris Est Creteil, F-77474 Marne-la-Vallée, France*

Abstract

The problem addressed in this paper concerns the frictional contact between an elastomer and a rigid body with randomly rough surfaces. The work is accomplished on the basis of two crucial elements: a framework for generating random geometries and a robust frictional contact algorithm, both of which are realised in the approach of Isogeometric analysis (IGA) for its high accuracy and robustness. For the former, a new Isogeometric framework for random geometry modelling is proposed, which combines the random field generation based on Karhunen-Loève expansion theory with Non-Uniform Rational B-Spline (NURBS) interpolation method. For the latter, a mortar-based frictional contact algorithm in 2D large deformation regime is adopted incorporating a modified closest point projection method for detection of contact. Numerical experiments are conducted with several settings such as 'rough-smooth', 'smooth-rough' and 'rough-rough' contact, depending on which side of the contact pair the randomly rough surface belongs to. The ratio of the global coefficient of friction to the prescribed local one and the ratio of true contact area to the nominal contact area are characterised under these settings, and factors like the root mean square roughness and correlation length of the random surface and the external traction are discovered to have a significant influence on the two ratios.

Keywords: Isogeometric analysis, computational contact mechanics, rough surface, random geometry modelling

1. Introduction

Contact between rough surfaces has been a prevailing research topic for decades in many scientific subfields including tribology and computational mechanics. In the field of tribology, to name a few, pioneering work was conducted by Greenwood and Williamson [1], who proposed the famous GW model based on the assumption of independent hemisphere asperities in contact, which is still being investigated and modified for various applications [2]. Whitehouse and Archard [3] characterised a random profile by a Gaussian height distribution, indicating the root mean square (RMS) roughness and the correlation length as two

*Corresponding author
Email address: batoua@liverpool.ac.uk (Anas Batou)

important parameters. Persson [4, 5] proposed a contact theory based on the probability distribution of contact stresses, introducing surface roughness power spectrum as an inherent factor of rough surfaces. These analytical approaches, though succeeded in predicting deformation and contact area under specific scenarios, had limitations due to their simplified assumptions such as absence of mutual interactions of asperities or infinitesimal deformation during contact. On the other hand, in the field of computational mechanics, the use of numerical methods get boosted in tackling contact problems because of the growing computing power and advancement in algorithms, among which those reported in [6, 7] stand as outstanding representatives. The Finite Element Method (FEM), is arguably the most versatile numerical method in this category and is widely adopted in the literature. Various FEM-based contact formulations have been developed, such as Node-to-Segment (NTS) formulation [8], Segment-to-Segment (STS) formulation [9] and Mortar formulation [10]. These formulations in general can deal with small or large deformation, frictionless or frictional contact problems, and have their own merits and limitations. For an extensive overview of the use of FEM in computational contact mechanics, please refer to [11]. Alternatively, the Boundary Element Method (BEM) [12] and Fast Fourier Transformation (FFT) method [13] are also applicable of handling contact problems.

In recent decades, Isogeometric analysis (IGA) proposed by Hughes et al [14] to integrate the Computer Aided Geometric Design (CAGD) and the FEM, shows a promising capability in the treatment of contact problems. In IGA, Non-Uniform Rational B-Spline (NURBS) basis functions play the role of conventional shape functions in FEM. NURBS basis functions intrinsically possess higher-order and tailorable continuity, which enable IGA to not only represent precisely the complex geometry under investigation with a fairly coarse mesh but also lead to increased accuracy and robustness of the results in comparison to standard FEM. Furthermore, the higher continuity across elements makes IGA particularly suitable for contact treatment, as recognised already in the original IGA paper [14], which results in a smooth description of contacting profile or surface and more importantly provides a continuous normal field of the contacting interface. Thereby it avoids the necessity of using smoothing [15, 16] or normal averaging [17, 18] techniques, which are often required in the context of FEM. Consequently, these superiors properties facilitate the derivation of a variationally consistent formulation in an iterative nonlinear framework.

Early attempts applying IGA to contact problems can be found in Temizer et al [19], Lorenzis et al [20], Lu [21] and Kim et al [22] and a comprehensive review of Isogeometric contact can be found in [23]. Temizer et al [19] developed a three-dimensional frictionless knot-to-surface algorithm (as an analogy to the NTS algorithm) and obtained reliable results of the classical Hertzian contact problem. The over-constraint phenomena were observed and a mortar-based constraint relaxation technique was proposed. Temizer et al [24] extended that algorithm to the three-dimensional mortar-based frictional contact treatment in the regime of finite deformation. Lorenzis et al [20] presented a two-dimensional large deformation frictional mortar contact formulation using NURBS discretisation. The significant superiority of its performance over the contact formulation based on Lagrangian basis functions was found as the latter displayed irregular

contact force oscillations. The formulation was further extended to a three-dimensional frictionless case by Lorenzis et al [25], with the augmented Lagrangian method utilised in the iterative solver. Matzen et al [26] proposed a point-to-segment algorithm, in which the Lagrange multiplier method was used in the contact formulation and Greville and Botella points were chosen as collocation points for the evaluation of contact integrals. An extension to three-dimensional problems termed a weighted point-based contact approach was recently proposed by Matzen et al [27]. An unbiased two-half-pass contact algorithm was proposed by Sauer and Lorenzis [28], of which the derivation was based on surface potentials [29] and counted both the master and slave side contributions into the contact integrals. The extension of the two-half-pass contact algorithm to a segmentation-free mortar contact formulation was presented by Duong et al [30]. And a varying-order NURBS discretisation technique incorporated in the two-half-pass algorithm to refine the contacting boundary of the geometry with order elevation while keeping the bulk parameterisation unchanged, was presented by Agrawal and Gautam [31], in which higher accuracy and efficiency was achieved. Apart from the above Galerkin-based IGA formulations, an alternative approach [32, 33] to solve contact problems is to collocate the strong form of the original boundary value problem, which leads to a significant reduction of computational time.

Despite the power of IGA in geometry modelling and the existence of a variety of contact algorithms, their use in the contact problems of randomly rough surfaces are rarely seen in the literature, and a consistent IGA framework for generating random geometry is still missing. To list the only few relevant published works, Temizer [34] established an IGA-based contact homogenisation framework towards contact problems between periodically and randomly rough elastic boundary layers. Investigations on characterising the global coefficient of friction were conducted in the sense of varying the geometry, material and load parameters. The results revealed the influence of microscopic roughness on the global coefficient of friction by demonstrating that it might be feasible to assign a well-defined global coefficient of friction to a contact interface with random roughness but impossible for one with periodic roughness. In a following investigation, Kılıç and Temizer [35] proposed a tuning approach towards the mean value and oscillation of macroscopic frictional response of the contact interface with periodic bilateral roughness of elastic soft materials. They found that surface heterogeneities such as texture and bulk heterogeneities such as particle embedding can be applied individually or suppositionally in tuning the macroscopic frictional response in a finite deformation setting, by which a minimal oscillation of the magnitude of the macroscopic coefficient of friction was achievable. Tong et al [36] argued that the global coefficient of friction (COF) may differ from locally assumed COF because of large contact angles. They justified the findings through a single asperity contact model as well as a multi-asperity contact model.

In the present paper, a new IGA-based framework for random geometry modelling is proposed to facilitate the incorporation of roughness to contact surfaces, which integrates random field generation using Karhunen-Loève expansion (K-L expansion) and NURBS interpolation method. An adapted mortar-based frictional contact algorithm for elastic-rigid contact problems is developed using the penalty method. Numerical

experiments are performed based on whether the roughness is assigned to a single elastic or rigid surface or both. A local COF is prescribed to the contact interface and particular attention is paid to the effective global COF compared with the local one. Parametric analyses are conducted regarding RMS, correlation lengths of the surface and the external normal force. The remaining contents are organised as follows. In Sec.2 the IGA framework for the modelling of random geometry is proposed, comprising a brief introduction of fundamentals of IGA, the IGA random field modelling method and NURBS interpolation method. A frictional contact algorithm dealing with 2D elastic-rigid contact problem in the large deformation regime is presented in Sec.3. Numerical experiments with regard to three basic settings, namely 'rough-smooth' contact, 'smooth-rough' contact and 'rough-rough' contact, are reported in Sec.4. Lastly, Sec.5 concludes and closes the paper.

2. Isogeometric framework for random geometry modelling

2.1. Preliminaries

In this section, the fundamentals of IGA are briefly reviewed, starting with B-spline and NURBS basis functions, and then describing their uses in the representation of geometries. For a full description, interested readers are referred to the original paper by Hughes [14] and the monograph [37]. A B-spline of degree p is built upon a non-decreasing knot vector $\Xi = \{\xi_1, \xi_2, ..., \xi_{n+p+1}\}$, where ξ_i is the i-th knot entry and n is the total number of the B-spline basis functions. A p-th degree univariate B-spline basis function $N_{i,p}$ can be obtained recursively through the Cox-de Boor formula [38]. For $p = 0$

$$N_{i,0}(\xi) = \begin{cases} 1 & \xi_i \leq \xi < \xi_{i+1} \\ 0 & \text{otherwise} \end{cases} . \tag{1}$$

For a positive integer p

$$N_{i,p}(\xi) = \frac{\xi - \xi_i}{\xi_{i+p} - \xi_i} N_{i,p-1}(\xi) + \frac{\xi_{i+p+1} - \xi}{\xi_{i+p+1} - \xi_{i+1}} N_{i+1,p-1}(\xi) \ . \tag{2}$$

These B-spline basis functions are piecewise polynomials exhibiting a few properties worthy of noting, which are (1) partition of unity, i.e. $\sum_{i=1}^{p+1} N_{i,p}(\xi) = 1$; (2) non-negativity, i.e. $N_{i,p}(\xi) \geq 0$; (3) linear independence; (4) knot multiplicity dependent continuity, i.e. the basis functions are C^{p-k}-continuous at the internal knot (knot other than the first and last knot) whose multiplicity is k. When $k = p$ the basis functions are C^0 continuous across that knot thus interpolatory at the location. In particular, a knot vector with its first and last knot entries repeated by $p + 1$ times is called an *open vector*. And basis functions defined on an open vector are interpolatory at the boundaries.

Multivariate B-splines are achieved by the tensor product of univariate B-splines with their basis functions denoting as

$$N^{(d_s)}_{\boldsymbol{i},\boldsymbol{p}}(\boldsymbol{\xi}) = \prod_{d=1}^{d_s} N^{(1)}_{i_d,p_d}(\xi^d) \ , \tag{3}$$

where d_s is the dimension of the multivariate B-splines, $\boldsymbol{i} = \{i_1, ..., i_{d_s}\}$, $\boldsymbol{p} = \{p_1, ..., p_{d_s}\}$ and $\boldsymbol{\xi} = \{\xi^1, ..., \xi^{d_s}\}$ indicate the index number, spline degree and parametric coordinate in each dimension of the multivariate B-splines, respectively. $N^{(1)}_{i_d,p_d}(\xi^d)$ is the univariate B-spline basis function of the dimension d. In this case, a B-spline geometry can be represented as

$$\mathbf{G}_B(\boldsymbol{\xi}) = \sum_{\boldsymbol{i}} N^{(d_s)}_{\boldsymbol{i},\boldsymbol{p}}(\boldsymbol{\xi})\, \mathbf{P}_{\boldsymbol{i}} \ , \tag{4}$$

where $\mathbf{G}_B(\boldsymbol{\xi})$ can be a curve, a surface or a volume depending on the dimension d_s. $\mathbf{P}_{\boldsymbol{i}} \in \mathbb{R}^{d_s}$ are the corresponding control points, of which the number is the same as that of the (multivariate-) B-spline basis functions. NURBS are generalisations of B-splines that possess merits of flexibility and accuracy in the modelling geometries of arbitrary shapes. NURBS basis functions are defined through rational weighted B-spline basis functions as

$$R^{(d_s)}_{\boldsymbol{i},\boldsymbol{p}}(\boldsymbol{\xi}) = \frac{N^{(d_s)}_{\boldsymbol{i},\boldsymbol{p}}(\boldsymbol{\xi})\ \omega_{\boldsymbol{i}}}{W(\boldsymbol{\xi})} = \frac{N^{(d_s)}_{\boldsymbol{i},\boldsymbol{p}}(\boldsymbol{\xi})\ \omega_{\boldsymbol{i}}}{\sum_{\boldsymbol{j}} N^{(d_s)}_{\boldsymbol{j},\boldsymbol{p}}(\boldsymbol{\xi})\ \omega_{\boldsymbol{j}}} \ , \tag{5}$$

where $N^{(d_s)}_{\boldsymbol{i},\boldsymbol{p}}(\boldsymbol{\xi})$ are the (multivariate-) B-spline basis functions and $\omega_{\boldsymbol{i}} > 0$ are the NURBS weights. Similar to B-spline geometries, a NURBS geometry can be formed as

$$\mathbf{G}_N(\boldsymbol{\xi}) = \sum_{\boldsymbol{i}} R^{(d_s)}_{\boldsymbol{i},\boldsymbol{p}}(\boldsymbol{\xi})\, \mathbf{P}_{\boldsymbol{i}} \ . \tag{6}$$

Similarly, $G_N(\boldsymbol{\xi})$ can be a curve, a surface or a volume depending on d_s and $\mathbf{P}_{\boldsymbol{i}} \in \mathbb{R}^{d_s}$ are the corresponding control points. The authors note that (6) is defined on the parametric space and can be seen as a mapping from the parametric domain to the physical domain. The NURBS functions in the physical domain can thus be obtained through a push-forward method as $\bar{R}^{(d_s)}_{\boldsymbol{i},\boldsymbol{p}}(\mathbf{x}) := R_{\boldsymbol{i},\boldsymbol{p}}(\boldsymbol{\xi})^{(d_s)} \circ \boldsymbol{x}^{-1}$.

2.2. Isogeometric random field modelling

Random field generation methods in Isogeometric framework have recently been proposed based on Karhunen-Loève expansion (KL-expansion) in [39] and [40]. Essentially, both methods solve a Fredholm integral eigenvalue problem while they are distinguished in treatments to approximate the solution through Galerkin or collocation projection. As argued in [40], the Galerkin projection method suffers severe computational inefficiencies because of dimension explosion in the construction of the system matrix. In contrast, the collocation method solves the strong form directly with collocated points instead of requiring a weak form of the original eigenvalue problem. Its realisation benefits from the high continuity of NURBS in Isogeometric analysis, which makes it more promising in practical applications. In the following, first the basic theory of KL expansion is briefly introduced and then the collocation method is introduced in solving the KL approximation problem in the Isogeometric problem. Finally, two numerical examples corresponding to 1D and 2D random field are presented.

2.2.1. Karhunen-Loève expansion

Let α denote a real-valued random field defined on a closed bounded domain $\mathcal{D} \subset \mathbb{R}^d$, where $d = 1, 2$ or 3 indicating a mapping $\alpha : \mathcal{D} \times \Omega \to \mathbb{R}$ and $\alpha(\mathbf{x}, \Theta)$ is a random variable for each $\mathbf{x} \in \mathcal{D}$ and $\Theta \in \Omega$ with respect to a complete probability space $(\Omega, \mathcal{F}, \mathbb{P})$, where Ω is a sample space, $\mathcal{F}$ is a σ-algebra on Ω and $\mathbb{P}$ is a probability measure. The covariance function of $\alpha(\mathbf{x}, \cdot)$ is defined by

$$C(\mathbf{x}, \mathbf{x}') := \mathbb{E}[(\alpha(\mathbf{x}, \Theta) - \mu_{\mathbf{x}})(\alpha(\mathbf{x}', \Theta) - \mu_{\mathbf{x}}))], \ \mathbf{x}, \mathbf{x}' \in \mathcal{D} \ , \tag{7}$$

where $\mathbb{E}$ is the expectation operator with respect to the probability measure $\mathbb{P}$, and $\mu_{\mathbf{x}} := \mathbb{E}[\alpha(\mathbf{x}, \Theta)]$ is the mean function. Without loss of generality, we assume that the mean value is zero, e.g. $\mu_{\mathbf{x}} = 0$ and the non-zero mean case can be represented by simply adding the mean value to the zero mean case. The random field is assumed to be homogeneous and isotropic, which mean that the covariance function $C(\mathbf{x}, \mathbf{x}')$ is a function of the distance $\|\mathbf{x} - \mathbf{x}'\|$. The covariance function $C(\mathbf{x}, \mathbf{x}')$ is bounded, symmetric and positive definite by definition. According to the theory of KL expansion [41], it has the spectral decomposition

$$C(\mathbf{x}, \mathbf{x}') = \sum_{n=0}^{\infty} \lambda_i \phi_i(\mathbf{x}) \phi_i(\mathbf{x}') \ , \tag{8}$$

where λ_i and $\phi_i(\mathbf{x})$ are the eigenvalues and eigenvectors of the covariance kernel, respectively. They are the solutions of the so-called Fredholm integral equation of the second kind as

$$\int_{\mathcal{D}} C(\mathbf{x}, \mathbf{x}') \phi_i(\mathbf{x}') \ \mathrm{d}\mathbf{x}' = \lambda_i \phi_i(\mathbf{x}) \ . \tag{9}$$

Moreover, the eigenfunctions form an orthogonal and complete set. They can be normalised according to $\int_{\mathcal{D}} \phi_i(\mathbf{x}) \phi_j(\mathbf{x}) d\mathbf{x} = \delta_{ij}$. The random field admits a convergent infinite series expansion as

$$\alpha(\mathbf{x}, \Theta) \sim \sum_{i=1}^{\infty} \sqrt{\lambda_i} \phi_i(\mathbf{x}) \theta_i \ , \tag{10}$$

where $\{\theta_i\}_{i \in \mathbb{N}}$ is an infinite sequence of random variables satisfying $\mathbb{E}[\theta_i] = 0$ and $\mathbb{E}[\theta_i \theta_j] = \delta_{ij}$. In practice, a finite number of the expansion terms is required and thus a truncation to a term N should be imposed, with the eigenvalues being rearranged in a descending sequence as

$$\alpha_N(\mathbf{x}, \Theta) = \sum_{i=1}^{N} \sqrt{\lambda_i} \phi_i(\mathbf{x}) \theta_i \ , \tag{11}$$

It has been proven that the KL approximation in (11) is optimal among all series expansion methods with respect to a global mean error. For the error analysis of (11), see [41].

2.2.2. Isogeometric collocation method

The analytical solutions of the eigenvalue problems in KL approximation (9) may only exist with restrictions, for example, the covariance function is separable and of a simple form or the domain $\mathcal{D}$ is rectangular. For general covariance functions or complex domains, the eigenvalue problems requires numerical methods.

Conventional numerical methods such as Galerkin methods and Nyström method can be found in the literature [42]. In this section, a collocation method is introduced in the Isogeometric framework to solve the eigenvalue problems.

Denote $\mathcal{C}(\mathcal{D})$ as a space of continuous functions on $\mathcal{D}$ with the supremum or uniform norm $\|\cdot\|_\infty$ and denote $\{\mathcal{S}_h\}_{h>0}$ as a sequence of approximating subspace of $\mathcal{C}(\mathcal{D})$ with finite dimension d_h. A residual can be defined as

$$\mathcal{R}^h := \int_{\mathcal{D}} C(\mathbf{x},\mathbf{x}')\phi^h(\mathbf{x}')\ \mathrm{d}\mathbf{x}' - \lambda^h\phi^h(\mathbf{x})\ , \tag{12}$$

where $\lambda^h \in \mathbb{R}^+$ and $\phi^h(\mathbf{x}) \in \mathcal{S}_h$. In the Isogeometric framework, we can find a sequence of univariate NURBS basis function as a basis of $\mathcal{S}_h$ (for a rigorous proof, see [40]), e.g. $\mathcal{S}_h = span\{\bar{R}^{(d_s)}_{J,\boldsymbol{p}}\}_{J=1}^{d_h} \subset \mathcal{C}(\mathcal{D})$, where I is the index number of $\bar{R}^{(d_s)}_{\boldsymbol{i},\boldsymbol{p}}$ depending on the dimension d_s of the domain $\mathcal{D}$ such that when $d_s = 1$, $J = i_1$; when $d_s = 2$, $J = (i_2 - 1) \times n_1$; and when $d_s = 3$, $J = (i_3 - 1) \times n_1 n_2 + (i_2 - 1) \times n_1 + i_1$, where n_d is the number of NURBS basis functions in the direction $d \in \{1, 2, 3\}$. In this case, the eigenfunction $\phi^h(\mathbf{x})$ can be represented through a linear combination of $\{\bar{R}^{(d_s)}_{I,\boldsymbol{p}}\}_{J=1}^{d_h}$ as

$$\phi^h(\mathbf{x}) = \sum_{J=1}^{d_h} f_J \bar{R}_{J,\boldsymbol{p}}(\mathbf{x})\ , \tag{13}$$

where $f_J \in \mathbb{R}$ are the coefficients. The superscript (d_s) of the NURBS basis functions are omitted for convenience. The residual can be obtained by substituting (13) into (12) as

$$\mathcal{R}^h = \sum_{J=1}^{d_h} f_J \Big[\int_{\mathcal{D}} C(\mathbf{x},\mathbf{x}')\bar{R}_{J,\boldsymbol{p}}(\mathbf{x}')\ \mathrm{d}\mathbf{x}' - \lambda^h \bar{R}_{J,\boldsymbol{p}}(\mathbf{x}) \Big]\ , \tag{14}$$

The key idea of the collocation method is to select distinct collocation points such that the residual (14) vanishes at those points and the problem is then converted to a generalised eigenvalue problem to solve for the coefficients f_J. The collocation points to be selected $\mathbf{x}_J \in \mathcal{D}$ should satisfy certain requirements such that the existence and uniqueness of the solution are guaranteed, as

$$\det\big[\bar{R}_{J,\boldsymbol{p}}(\mathbf{x}_I)\big] \neq 0,\ I, J = 1, ..., d_h\ . \tag{15}$$

A widely used strategy for the determination of collocation points is to enforce the mapping of the Greville abscissae [43] in the parametric space to the physical space. The Greville abscissae $\bar{\xi}^k_{J_k}, J_k = 1, ..., n_k$ of the kth coordinate direction of the parametric domain $\bar{\mathcal{D}} = [0, 1]^{d_s}, k = 1, ..., d_s$ are defined from the knot vector as

$$\bar{\xi}^k_{I_k} := \frac{1}{p_k} \sum_{q=1}^{p_k} \xi^k_{I_k+q}\ , \tag{16}$$

where n_k is the number of collocation points in the kth direction and $n_c = \prod_{k=1}^{d_s} n_k$ is the total number of collocation points. Note that $n_c = d_h$. Finally, the collocation points are defined as the image of the Greville abscissae as

$$\bar{\mathbf{x}}_I = \mathbf{x}(\boldsymbol{\xi}_I),\ \boldsymbol{\xi}_I = \{\xi^1_{I_1}, ..., \xi^{d_s}_{I_{d_s}}\} \in \bar{\mathcal{D}},\ \forall I_k \in \{1, ..., n_k\}\ . \tag{17}$$

The convergence and stability analysis of the Greville abscissae strategy has been presented in [40] for the one-dimensional case. Although not ready to be extended to higher dimensions, it is practically proved useful in those cases. Alternatively, other strategies, e.g. Demko abscissae [43], may also be applied.

2.2.3. Generalised eigenvalue problem

The residual (14) is set to zero at the collocation points introduced in the last section, as

$$\mathcal{R}_I^h = \sum_{J=1}^{n_c} f_J \Big[\int_{\mathcal{D}} C(\bar{\mathbf{x}}_I, \mathbf{x}') \bar{R}_{J,\boldsymbol{p}}(\mathbf{x}') \, \mathrm{d}\mathbf{x}' - \lambda^h \bar{R}_{J,\boldsymbol{p}}(\bar{\mathbf{x}}_I) \Big] = 0, \ I = 1, ..., n_c \ . \tag{18}$$

The collection of the equations (18) with respect to the index J yield a generalised eigenvalue problem, written into a matrix form as

$$\mathbf{A}\mathbf{f}^h = \lambda^h \mathbf{B}\mathbf{f}^h \ , \tag{19}$$

where λ^h and $\mathbf{f}^h$ are respectively the eigenvalues and eigenvectors to be sought. $\mathbf{A}, \mathbf{B} \in \mathbb{R}^{n_c \times n_c}$ are system matrices with components as

$$A_{IJ} = \int_{\mathcal{D}} C(\bar{\mathbf{x}}_I, \mathbf{x}') \bar{R}_{J,\boldsymbol{p}}(\mathbf{x}') \, \mathrm{d}\mathbf{x}' \tag{20}$$

and

$$B_{IJ} = \bar{R}_{J,\boldsymbol{p}}(\bar{\mathbf{x}}_I) \ , \tag{21}$$

where $I, J = 1, ..., n_c$. Finally, the eigenfunctions in (13) are obtained as

$$\phi_I^h(\mathbf{x}) = \sum_{J=1}^{n_c} f_{I,J}^h \bar{R}_{J,\mathbf{p}}(\mathbf{x}), \ I = 1, ..., n_c \ , \tag{22}$$

where $f_{I,J}^h$ is the Jth component of the Ith eigenvector in the solution of (19) corresponding to the Ith eigenvalue λ_I^h, which is often sorted in a descending order according to their values.

2.2.4. Numerical examples of random field

In this section, 1D and 2D random fields are generated to illustrate the effectiveness of the method. For both examples, the exponential correlation function is used, which has the form of

$$R(\mathbf{x}, \mathbf{x}') = \mathrm{e}^{-\frac{\|\mathbf{x}-\mathbf{x}'\|}{l}} \ , \tag{23}$$

where l has the unit of length and is often termed 'correlation length'. The authors would like to note that other forms of correlation function, e.g. Gaussian and sinusoidal, are also applicable. The exponential function is a realistic description of surface roughness, and an additional advantage is that only this form of function leads to an analytical solution of 1D problem.

For the 1D case, a NURBS straight line is generated with length $L = 1$, degree $p = 2$ and initial knot vector $\{0, 0, 0, 1, 1, 1\}$. The final knot vector is obtained through a knot insertion refinement procedure [14] by adding 50 knot values equally spaced in $[0, 1]$ to the initial knot vector. The collocation points derived through (16) and (17) are shown as red dots in Fig.1a. The correlation length is set to $l = 0.1$. The first five

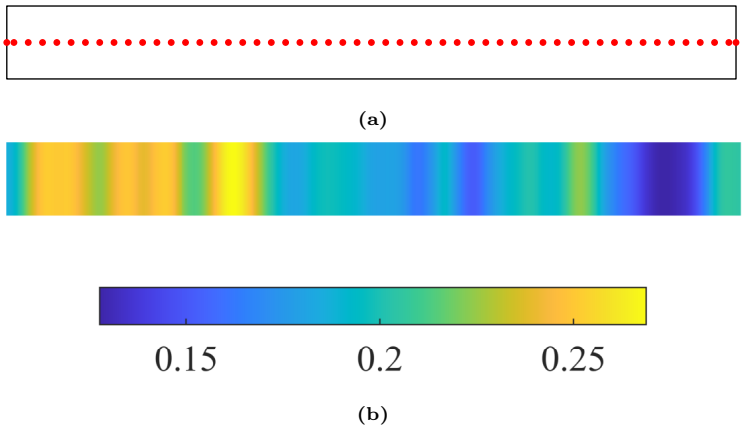

Fig. 1. 1D case. (a) Collocation points; (b) Random field.

Table 1: First five eigenvalues of 1D problem

Order	Numerical solution λ_n^h	Analytical solution λ	Relative error err
1	0.18713553	0.18708255	2.8317158 e-4
2	0.15609842	0.15604556	3.3875399 e-4
3	0.12120695	0.12115435	4.3414122 e-4
4	0.09137638	0.09132424	5.7094505 e-4
5	0.06878706	0.06873560	7.4879421 e-4

eigenvalues calculated through numerical method λ_n^h are compared to the analytical solutions λ_n, which are elucidated in [41] and in Table.1. The relative error in the table is defined as

$$\text{err} = \frac{\|\lambda_n - \lambda_n^h\|}{\lambda_n}. \tag{24}$$

As shown in Table.1, the numerical-analytical relative errors of the first five eigenvalues are below 0.1%, thus proving the effectiveness of the numerical method. The eigenfunctions corresponding to the first five eigenvalues of the numerical results are compared with their analytical counterparts in Fig.2, in which the degree numbers are marked close to the curve. These results are in good consistency. Finally, the generated 1D random field is presented in Fig.1b. A further inspection of the validity of the current method to generate a consistent correlation structure and height distribution is performed in Appendix B.

For the 2D case, the procedure to model a random field is almost the same with only differences in replacing the 1D NURBS basis functions by its 2D version and collocating points in the 2D rather than 1D space. A NURBS circle is used to illustrate the collocation points used to derive eigen information in Fig.3a and one realisation of the random field is shown in Fig.3b. Unlike 1D case, no analytical result is available. It should be noted that a merit of the IGA collocation method is that once the eigen information is obtained, the random realisations of any point in the geometry domain can be obtained straightforwardly

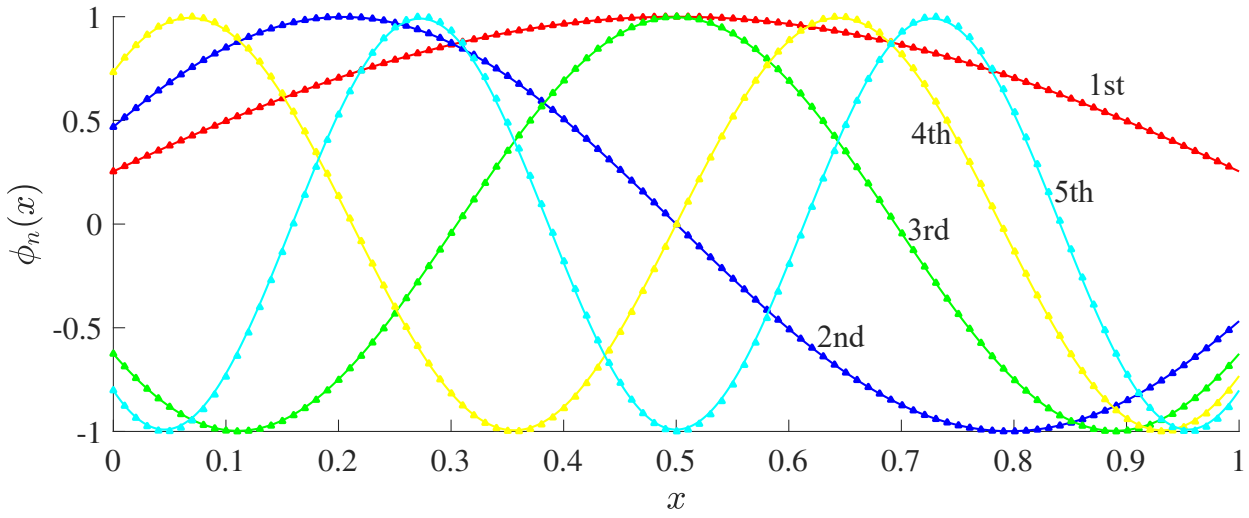

Fig. 2. First five eigenfunctions of 1D problem, line - numerical solution; triangle - analytical solution.

without the need of remeshing or interpolation used in other random field generation methods. On the other hand, efficiency is sacrificed as the process of setting and solving the generalised eigenvalue problem can be time-consuming.

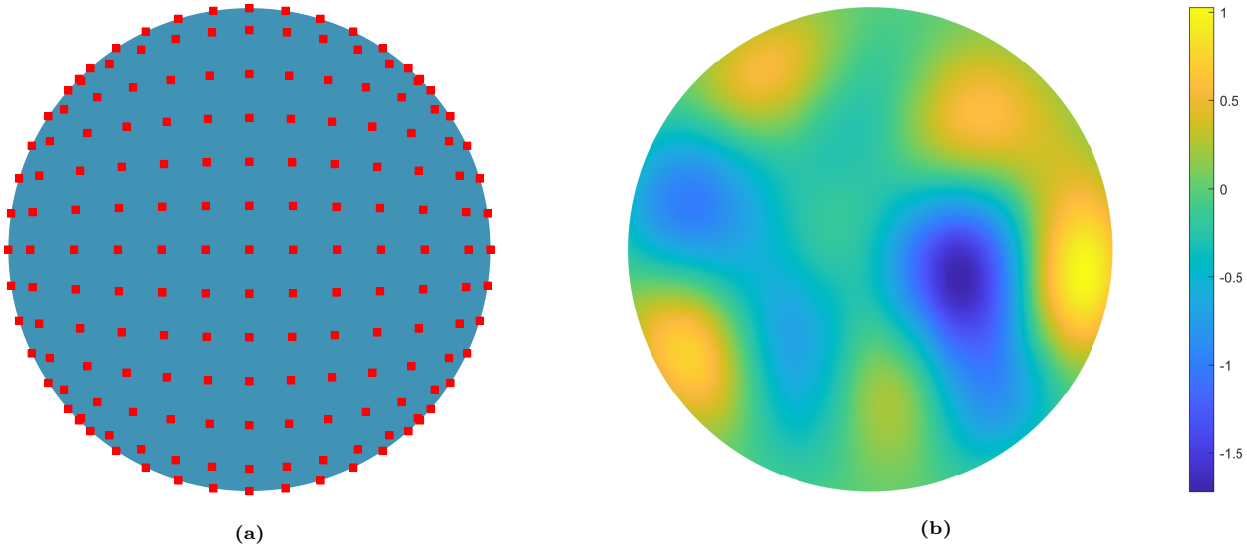

Fig. 3. 2D case. (a) Collocation points; (b) Random field.

2.3. Isogeometric random geometry modelling

The random geometry can be constructed by incorporating the random field into an existing deterministic NURBS geometry, e.g. a 1D random field can be incorporated as the random profile of 2D geometry and a 2D random field as the random surface of 3D geometry. This incorporation can be accomplished by the NURBS curve interpolation and surface interpolation method [44]. In the following, these interpolation methods

are first introduced and then used to extend the random fields generated in Sec.2.2.4 to the corresponding NURBS random geometries.

2.3.1. NURBS curve and surface interpolation

NURBS curve interpolation is an inverse procedure of the NURBS curve generation. Recall (6) in the 1D case that a sequence of interpolation points $\{Q_k\}_{k=1}^N$ of the random field are known as

$$Q_k = G_N(\bar{\xi}_k) = \sum_{i=1}^{N} P_i R_{i,p}(\bar{\xi}_k),\ k = 1, \ldots, N, \tag{25}$$

where $\bar{\xi}_k$ is the inverse image of Q_k in the parametric space $[0, 1]$, $R_{i,p}$ are the ith 1-D NURBS basis functions of the degree p and P_i are the coordinates of the corresponding control points. Equations (25) can be rearranged in a matrix form as

$$\begin{bmatrix} R_{1,p}(\bar{\xi}_1) & \cdots & R_{N,p}(\bar{\xi}_1) \\ R_{1,p}(\bar{\xi}_2) & \cdots & R_{N,p}(\bar{\xi}_2) \\ \vdots & \ddots & \vdots \\ R_{1,p}(\bar{\xi}_N) & \cdots & R_{N,p}(\bar{\xi}_N) \end{bmatrix} \begin{bmatrix} P_1 \\ P_2 \\ \vdots \\ P_N \end{bmatrix} = \begin{bmatrix} Q_1 \\ Q_2 \\ \vdots \\ Q_N \end{bmatrix}. \tag{26}$$

In order to solve for $\{P_i\}_{i=1}^N$, the collocated parametric coordinates $\{\bar{\xi}_k\}_{k=1}^N$ are to be decided. The choice of those knots should meet the invertible constraint like (15) as

$$\det\big[R_{i,p}(\bar{\xi}_k)\big] \neq 0,\ i, k = 1, \ldots, N. \tag{27}$$

One possible strategy is the chord length method [45] and it determines the sequence of the collocated knots recursively through

$$\bar{\xi}_k = \bar{\xi}_{k-1} + \frac{|Q_k - Q_{k-1}|}{\sum_{j=1}^{N} |Q_j - Q_{j-1}|},\ \bar{\xi}_1 = 0 \text{ and } \bar{\xi}_N = 1. \tag{28}$$

Finally, the knot vector required for the modelling of the random profile can be defined through a local average of the collocated knots as

$$\mathbf{U} = \{\underbrace{\xi_1, \cdots, \xi_{p+1}}_{=0}, \xi_{p+2}, \cdots, \xi_N, \underbrace{\xi_{N+1}, \cdots, \xi_{N+p+1}}_{=1}\},\ \text{where } \xi_{k+p} = \frac{1}{p} \sum_{l=k}^{k+p-1} \bar{\xi}_l \text{ for } k = 2, \ldots, N-p. \tag{29}$$

The NURBS surface interpolation can be conducted similarly. The difference lies in the sequence of interpolation points having an additional index for the second direction, e.g. $\{Q_{k,l}\}$, $k = 1, \ldots, N$ and $l = 1, \ldots, M$, and a control net and knot vectors in both directions are to be determined. The relation between $\{Q_{k,l}\}$ and the control net $\{P_{i,j}\}$ is

$$Q_{k,l} = G_N(\bar{\xi}_k^1, \bar{\xi}_l^2) = \sum_{i=1}^{N} \sum_{j=1}^{M} P_{i,j} R_{\boldsymbol{i},\boldsymbol{p}}^{(2)}(\bar{\xi}_k^1, \bar{\xi}_l^2),\ k = 1, \ldots, N,\ l = 1, \ldots, M. \tag{30}$$

Unit weights are assumed so that the 2D NURBS basis functions can be represented as tensor products of their 1D counterparts, e.g. $R^{(2)}_{\boldsymbol{i},\boldsymbol{p}}(\bar{\xi}^1_k,\bar{\xi}^2_l) = R_{i_1,p_1}(\bar{\xi}^1_k)R_{i_2,p_2}(\bar{\xi}^2_l)$, and (30) can be written in a matrix form as

$$\begin{bmatrix} R_{1,p_1}(\bar{\xi}^1_1) & \cdots & R_{N,p_1}(\bar{\xi}^1_1) \\ \vdots & \ddots & \vdots \\ R_{1,p_1}(\bar{\xi}^1_N) & \cdots & R_{N,p_1}(\bar{\xi}^1_N) \end{bmatrix} \begin{bmatrix} P_{1,1} & \cdots & P_{1,M} \\ \vdots & \ddots & \vdots \\ P_{N,1} & \cdots & P_{N,M} \end{bmatrix} \begin{bmatrix} R_{1,p_2}(\bar{\xi}^2_1) & \cdots & R_{1,p_2}(\bar{\xi}^2_M) \\ \vdots & \ddots & \vdots \\ R_{M,p_2}(\bar{\xi}^2_1) & \cdots & R_{M,p_2}(\bar{\xi}^2_M) \end{bmatrix} = \begin{bmatrix} Q_{1,1} & \cdots & Q_{1,M} \\ \vdots & \ddots & \vdots \\ Q_{N,1} & \cdots & Q_{N,M} \end{bmatrix}. \tag{31}$$

The collocated knot pairs $\{\bar{\xi}^1_k,\bar{\xi}^2_l\}$ are determined through the following strategy [44].

$$\begin{aligned} \bar{\xi}^1_{k,l} &= \bar{\xi}^1_{k-1,l} + \frac{|Q_{k,l}-Q_{k-1,l}|}{\sum_{j=1}^{N}|Q_{j,l}-Q_{j-1,l}|},\ \bar{\xi}^1_{1,l}=0 \text{ and } \bar{\xi}^1_{N,l}=1 \text{ and } \bar{\xi}^1_k = \frac{1}{M}\sum_{l=1}^{M}\bar{\xi}^1_{k,l}\ , \\ \bar{\xi}^2_{l,k} &= \bar{\xi}^2_{l-1,k} + \frac{|Q_{k,l}-Q_{k,l-1}|}{\sum_{j=1}^{M}|Q_{k,j}-Q_{k,j-1}|},\ \bar{\xi}^2_{1,k}=0 \text{ and } \bar{\xi}^2_{M,k}=1 \text{ and } \bar{\xi}^2_l = \frac{1}{N}\sum_{k=1}^{N}\bar{\xi}^2_{l,k}. \end{aligned} \tag{32}$$

It should be noted in this strategy that the collocated knots in each direction also satisfy the constraint (27). Finally, the knot vector for each direction can be obtained by (33), respectively as

$$\begin{aligned} \mathbf{U} &= \{\underbrace{\xi^1_1,\cdots,\xi^1_{p_1+1}}_{=0},\xi^1_{p_1+2},\cdots,\xi^1_N,\ \underbrace{\xi^1_{N+1},\cdots,\xi^1_{N+p_1+1}}_{=1}\},\ \text{where } \xi^1_{k+p_1} = \frac{1}{p_1}\sum_{l=k}^{k+p_1-1}\bar{\xi}^1_l \text{ for } k=2,\ldots,N-p_1 \\ \mathbf{V} &= \{\underbrace{\xi^2_1,\cdots,\xi^2_{p_2+1}}_{=0},\xi^2_{p_2+2},\cdots,\xi^2_M,\ \underbrace{\xi^2_{M+1},\cdots,\xi^2_{M+p_2+1}}_{=1}\},\ \text{where } \xi^2_{l+p_2} = \frac{1}{p_2}\sum_{k=l}^{l+p_2-1}\bar{\xi}^2_k \text{ for } l=2,\ldots,M-p_2 \end{aligned} \tag{33}$$

2.3.2. Numerical examples of random geometry

The results of Sec.2.2.4 are used in this section to generate random geometries. Moreover, an 'extrusion' procedure is applied to the original random field by adding one to its dimension, i.e. a 1D random field is incorporated in the model as the random profile of a 2D geometry and a 2D random field is incorporated in the model as the random surface of a 3D geometry, as shown in Fig.4. This procedure is straightforward to implement, for instance, by defining a knot vector $\mathbf{W}=\{0,0,1,1\}$ and corresponding control points in the additional dimension. In this way, a geometry with randomly rough edge (profile or surface) can be constructed.

3. Large deformation frictional elastic-rigid contact algorithm

In this section, the contact algorithm and implementation details are presented for tackling 2D large deformation elastic-rigid frictional contact problems. The algorithm is readily developed from [20] for general 2D elastic contact problems and is adopted here with some modifications. The authors note that here the analysis is restricted to 2D, but the extension to an elastic-elastic contact problem in 3D is feasible with additional algorithmic complexities, for which the details can be found in [25, 28, 27]. For more details and more general topics on contact problems, see [6] and [7].

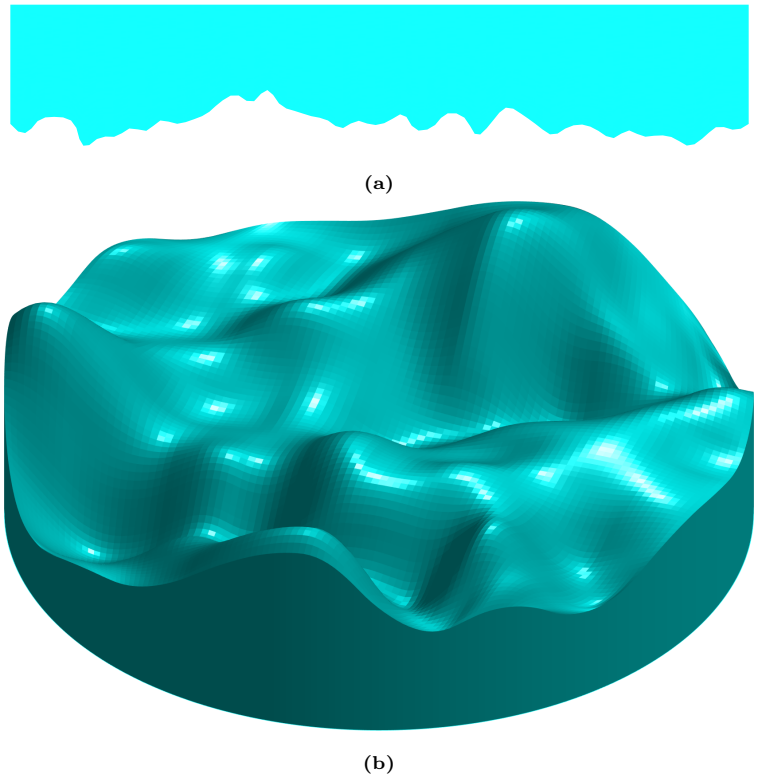

Fig. 4. Random geometries. (a) 2D geometry with random profile; (b) 3D geometry with random surface.

3.1. Problem definition

An elastic body is set to contact with a fixed rigid ground, as illustrated in Fig.5. The conventional 'slave-master' terminology is used in this work such that the elastic body is termed as slave body, denoted by $\mathcal{B}^s$, and the rigid ground is termed as the master body, denoted by $\mathcal{B}^m$. The boundary of the domain ($\partial\mathcal{B}^i = \Gamma_u^i \cup \Gamma_\sigma^i \cup \Gamma_c^i$ in the initial configuration and $\partial\mathcal{B}^i = \gamma_u^i \cup \gamma_\sigma^i \cup \gamma_c^i$ in the current configuration, $i \in \{s, m\}$) is formed by the composition of boundary parts with displacement, traction and contact constraints, respectively. The deformation of the bodies can be expressed as

$$\mathbf{x}^i = \phi^i(\mathbf{X}^i) = \mathbf{X}^i + \mathbf{u}^i \ , \tag{34}$$

where $i \in \{s, m\}$, and $\mathbf{x}^i$ and $\mathbf{X}^i$ indicate the coordinates of the material points in the current and reference configurations, respectively. $\mathbf{u}^i$ is the displacement field of body i. $\phi^i(\cdot)$ is the deformation mapping of body i from the reference configuration to the current configuration. Note that $\mathbf{x}^m = \mathbf{X}^i$ and $\mathbf{u}^i = \mathbf{0}$ since the master body is fixed.

To facilitate the description of the contact variables, the master surface is parameterised through the convective coordinate ξ that defines the covariant vector $\boldsymbol{\tau}_1 = \mathbf{x}^m_{,\xi}$. The contravariant vector is defined as $\boldsymbol{\tau}^1 := m^{11}\boldsymbol{\tau}_1 = \boldsymbol{\tau}_1/m_{11}$, where $m_{11} := \boldsymbol{\tau}_1 \cdot \boldsymbol{\tau}_1$ is the metric. The curvature is defined as $k_{11} := \mathbf{x}^m_{,\xi\xi} \cdot \mathbf{n}$, where $\mathbf{n} = \mathbf{n}^m(\xi) = \frac{\mathbf{e}_3 \times \boldsymbol{\tau}_1}{\|\mathbf{e}_3 \times \boldsymbol{\tau}_1\|}$ is the normal unit vector and $\mathbf{e}_3$ is the unit vector of the third dimension.

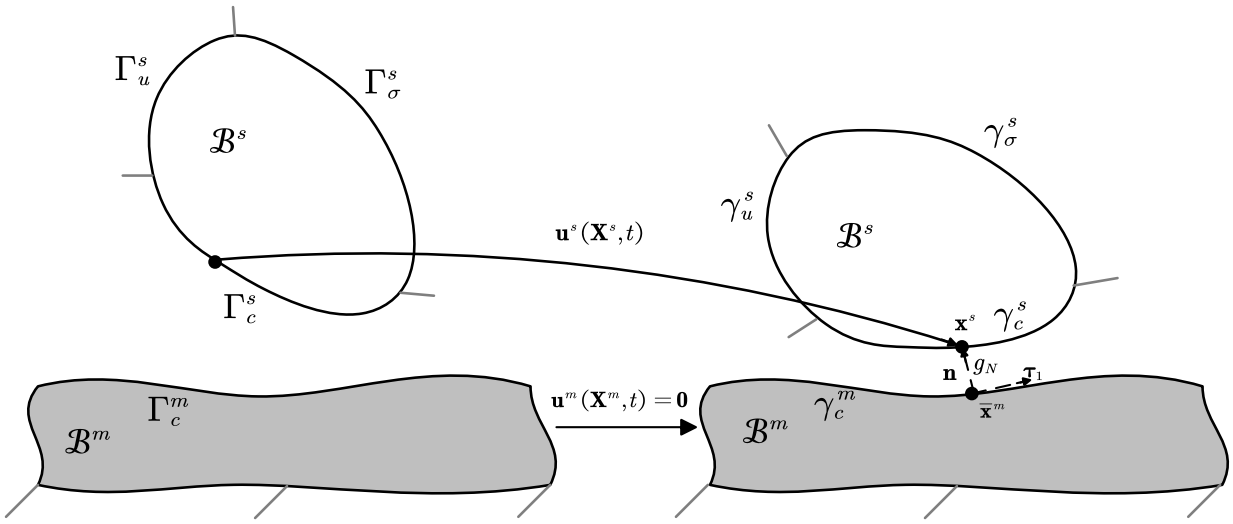

Fig. 5. Initial and current configurations of the contact problem

Denote γ_c as the contact interface in the current configuration where the contact occurs so that the contact interface of the slave surface and master surface coincide, e.g. $\gamma_c^s = \gamma_c^m = \gamma_c$. For the determination of γ_c, the distance function is introduced as

$$d := \|\mathbf{x}^s - \mathbf{x}^m(\xi)\| \,, \tag{35}$$

which describes the distance between a fixed point $\mathbf{x}^s$ on γ_c^s and an arbitrary point $\mathbf{x}^m = \mathbf{x}^m(\xi)$ on γ_c^m. Among those arbitrary points on γ_c^m, denote $\bar{\mathbf{x}}^m = \mathbf{x}^m(\bar{\xi})$ that minimises the distance function (35) as the projection of the slave point $\mathbf{x}^s$. The general procedure to determine the projection point usually involves the use of the Closest Point Projection (CPP) method, in which the solution is found through an optimisation approach minimising the distance function in (35), which is equivalent to finding the root of

$$f(\xi) := \boldsymbol{\tau}_1(\xi) \cdot [\mathbf{x}^s - \mathbf{x}^m(\xi)] \tag{36}$$

through Newton iterations. The CPP method works well for a generally smooth master surface. However, it may suffer severe numerical difficulties when random fluctuations are introduced in the master surface as the high local curvature may prevent the CPP method from convergence. Additionally, in such cases, the CPP method becomes intensively sensitive to the initialisation conditions and can be very time-consuming. Therefore, a modified genetic algorithm based on [46] is proposed in this work to determine the closest projection point, as summarised in Algorithm 1 below. Note that the input of $\bar{\xi}_n$ is used to accelerate the algorithm since the contact regions usually don't vary significantly between two adjacent time steps, which makes $\bar{\xi}_n$ a practical initial guess for the next time step. At the first time step, $\bar{\xi}_n$ is set to 0. From now on we use the over-bar sign, $(\bar{\bullet})$, to indicate a projected variable from a slave point.

Algorithm 1: A modified genetic algorithm to search for the closest projection point

Input : $MasterNurbsGeo$ - NURBS model of master surface;

$\mathbf{x}^s$ - position of the slave point;

$\bar{\xi}_n$ - projection parametric coordinate from the last time step.

Output: $\bar{\xi}$ - projection parametric coordinate from the current time step.

(1)**Initialisation**: Randomly generate a pool of N (N is an even number) parametric coordinates including $\bar{\xi}_n$ and sort them increasingly into a parent set as $\Sigma^p = \{\xi_1^p, \ldots, \xi_N^p\}$.

(2)**Create new generation**: Generate two sets of random variables $\{\alpha_I\}_{I=1}^{N/2}$, $\{\beta_J\}_{J=1}^{N/2}$ such that $0 \leq \alpha_I, \beta_J \leq 1$. Mate the nearest pair in the parent set Σ^p and produce two springs as

$$\begin{cases} \xi_i^s = \alpha_I \xi_i^p + (1-\alpha_I)\xi_{i+1}^p \\ \xi_{i+1}^s = \beta_J \xi_i^p + (1-\beta_J)\xi_{i+1}^p \end{cases} . \tag{37}$$

Then sort the springs into a spring set as $\Sigma^s = \{\xi_1^s, \ldots, \xi_N^s\}$.

(3)**Fitness evaluation**: The fitness of each point of two sets Σ^p, Σ^s are evaluated using (36), resulting in the evaluated parent set $\Theta^p = \{f(\xi_1^p), \ldots, f(\xi_N^p)\}$ and the evaluated spring set $\Theta^s = \{f(\xi_1^s), \ldots, f(\xi_N^s)\}$. Define $\Lambda = \min\{\Theta^p, \Theta^s\}$ as the minimum element of the two evaluated sets.

(4)**Resupply**: Keep the top K members of both sets Σ^p and Σ^s according to fitness evaluations and add M (such that $2K + M = N$) new randomly generated parametric points to form the parent set for the next iteration.

(5)**Convergence criteria**: The convergence criterion is set as $\Lambda < \epsilon$, where ϵ is the tolerance parameter. If the criterion is met, return $\bar{\xi} = f^{-1}(\Lambda)$. Repeat (1)$\sim$(5) if the criterion is not met.

3.2. Contact constraints

To form the contact constrains, the normal gap g_N is defined as

$$g_N = (\mathbf{x}^s - \bar{\mathbf{x}}^m) \cdot \mathbf{n} \ , \tag{38}$$

where $\mathbf{n} = \bar{\mathbf{n}}^m$ is the unit normal vector at the projection point of the master surface. The tangential gap in the incremental form by the use of backward time-discretised Euler formulation is defined as

$$\dot{\mathbf{g}}_T = \dot{\bar{\xi}} \boldsymbol{\tau}_1 \rightarrow \dot{\mathbf{g}}_T = (\bar{\xi} - \bar{\xi}_n)/\Delta t \ \boldsymbol{\tau}_1 \ , \tag{39}$$

where $\boldsymbol{\tau}_1 = \bar{\boldsymbol{\tau}}_1^m$ is the covariant vector at the projection point and $\bar{\xi}_n$ denotes the projection parametric coordinate of the same slave point at the last time step mentioned in Algorithm 1. In the following, all variables are by default assumed to be in the current time step, e.g. $t = t_{n+1}$, except for those with subscript n indicating the last time step, e.g. $t = t_n$.

The contact traction vector in the current configuration $\mathbf{t} = \mathbf{t}^m = -\mathbf{t}^s$ can be decomposed into its normal and tangential components as

$$\mathbf{t} = \mathbf{t}_N + \mathbf{t}_T = t_N \mathbf{n} + t_{T_1} \boldsymbol{\tau}^1. \tag{40}$$

Concerning unilateral contact with dry friction only, the Karush-Kuhn-Tucker (KKT) conditions for impenetrability in the normal direction are

$$g_N \geq 0,\ t_N \leq 0,\ g_N t_N = 0 \quad \dot{g}_N t_N = 0\ , \tag{41}$$

and the KKT conditions for Coulomb friction in the tangential direction are

$$\Phi = \|\mathbf{t}_T\| - \mu |t_N| \leq 0,\ \dot{\mathbf{g}}_T = \dot{\gamma} \frac{\mathbf{t}_T}{\|\mathbf{t}_T\|},\ \gamma \geq 0 \quad \gamma \Phi = 0\ , \tag{42}$$

where $\gamma = \dot{\gamma} \Delta t$ is the slip length and μ is the COF. The authors would like to note that according to the existing literature [47, 48], the COF is not always a material constant and may possess a significant amount of randomness. However, for computational convenience, in this work the static COF and kinetic COF are assumed to be the same constant.

The contact constrains are here regularised with penalty method as

$$t_N = \varepsilon_N \langle g_N \rangle_-\ ,\ \langle g_N \rangle_- = \begin{cases} g_N & \text{if } g_N \leq 0 \\ 0 & \text{otherwise} \end{cases}\ , \tag{43}$$

where $\varepsilon_N > 0$ is the normal penalty parameter. The tangential contact traction is regularised in the time-discretised setting, reads

$$t_{T_1} = t_{T_{1n}} + \varepsilon_T \Big[m_{11}(\bar{\xi} - \bar{\xi}_n) - \gamma \frac{t_{T_1}}{\|\mathbf{t}_T\|} \Big],\ \Phi \leq 0 \quad \gamma \geq 0 \quad \Phi \gamma = 0\ , \tag{44}$$

where $\varepsilon_T > 0$ is the tangential penalty parameter. The frictional traction can be updated with the classical return mapping algorithm in analogy to plasticity theory. The trial state of the frictional traction starts with a non-slip assumption, e.g. $\gamma = 0$, as

$$t_{T_1}^{\text{trial}} = t_{T_{1n}} + \varepsilon_T \Big[m_{11}(\bar{\xi} - \bar{\xi}_n) \Big],\quad \Phi^{\text{trial}} = \|\mathbf{t}_T^{\text{trial}}\| - \mu |t_N|\ , \tag{45}$$

and the final state is determined with respect to stick or slip by Φ^{trial} as

$$t_{T_1} = \begin{cases} t_{T_1}^{\text{trial}} & \text{if } \Phi^{\text{trial}} \leq 0 \\ -\mu |t_N| \frac{t_{T_1}^{\text{trial}}}{\|\mathbf{t}_T^{\text{trial}}\|} & \text{otherwise} \end{cases}\ . \tag{46}$$

3.3. Contact virtual work and linearisation

The contact virtual work is expressed as

$$\delta W_c = \int_{\Gamma_c} \Big[t_N \delta g_N + \mathbf{t}_T \cdot \delta \mathbf{g}_T \Big] \mathrm{d}\Gamma = \int_{\Gamma_c} \Big[t_N \delta g_N + t_{T_1} \delta \bar{\xi} \Big] \mathrm{d}\Gamma. \tag{47}$$

Note that the integral area Γ_c is the contact region in the reference configuration by a 'pull-back' operation of γ_c in order to facilitate the linearisation of the contact virtual work. This procedure is not strictly accurate but is shown not to affect the results [20]. The linearisation of (47) yields

$$\Delta\delta W_c = \int_{\Gamma_c} \Big[\Delta t_N \delta g_N + t_N \Delta\delta g_N + \Delta t_{T_1}\delta\bar{\xi} + t_{T_1}\Delta\delta\bar{\xi}\Big]\mathrm{d}\Gamma. \tag{48}$$

The variational terms in (47), as well as their linearised terms in (48), can be readily taken from [6] as

$$\delta g_N = (\delta\mathbf{u}^s - \delta\bar{\mathbf{u}}^m)\cdot\mathbf{n} \quad \delta\bar{\xi} = H^{11}\Big[(\delta\mathbf{u}^s - \delta\bar{\mathbf{u}}^m)\cdot\boldsymbol{\tau}_1 + g_N\mathbf{n}\cdot\delta\bar{\mathbf{x}}^m_{,\xi}\Big]. \tag{49}$$

$$\begin{aligned}\Delta\delta g_N = &-(\delta\bar{\mathbf{x}}^m_{,\xi}\Delta\bar{\xi} + \Delta\bar{\mathbf{u}}^m_{,\xi}\delta\bar{\xi} + \bar{\mathbf{x}}^m_{,\xi\xi}\Delta\bar{\xi}\delta\bar{\xi})\cdot\mathbf{n}\\ &+ \frac{g_N}{m_{11}}(\delta\bar{\mathbf{x}}^m_{,\xi} + \bar{\mathbf{x}}^m_{,\xi\xi}\delta\bar{\xi})\mathbf{n}\otimes\mathbf{n}(\Delta\bar{\mathbf{u}}^m_{,\xi} + \bar{\mathbf{x}}^m_{,\xi\xi}\Delta\bar{\xi}).\end{aligned} \tag{50}$$

$$\begin{aligned}\Delta\delta\bar{\xi} = H^{11}\Big[&-\boldsymbol{\tau}_1\cdot(\delta\bar{\xi}\Delta\bar{\mathbf{u}}^m_{,\xi} + \delta\bar{\mathbf{x}}^m_{,\xi}\Delta\bar{\xi}) - (\boldsymbol{\tau}_1\cdot\bar{\mathbf{x}}^m_{,\xi\xi} - g_N\mathbf{n}\cdot\bar{\mathbf{x}}^m_{,\xi\xi\xi})\delta\bar{\xi}\Delta\bar{\xi}\\ &+ g_N(\delta\bar{\mathbf{x}}^m_{,\xi\xi}\Delta\bar{\xi} + \Delta\bar{\mathbf{u}}^m_{,\xi\xi}\delta\bar{\xi})\cdot\mathbf{n} - (\delta\bar{\mathbf{x}}^m_{,\xi} + \bar{\mathbf{x}}^m_{,\xi\xi}\delta\bar{\xi})\cdot\boldsymbol{\tau}_1\Delta\bar{\xi}\\ &- (\Delta\bar{\mathbf{u}}^m_{,\xi} + \bar{\mathbf{x}}^m_{,\xi\xi}\Delta\bar{\xi})\cdot\boldsymbol{\tau}_1\delta\bar{\xi} + (\delta\mathbf{x}^s - \delta\bar{\mathbf{x}}^m)\cdot(\Delta\bar{\mathbf{u}}^m_{,\xi} + \bar{\mathbf{x}}^m_{,\xi\xi}\Delta\bar{\xi})\\ &+ (\Delta\mathbf{u}^s - \Delta\bar{\mathbf{u}}^m)\cdot(\delta\bar{\mathbf{x}}^m_{,\xi} + \bar{\mathbf{x}}^m_{,\xi\xi}\delta\bar{\xi})\Big],\end{aligned} \tag{51}$$

where $H_{11} = m_{11} - g_N k_{11}$ and $H^{11} = 1/H_{11}$. The linearisation of the contact tractions can be derived as

$$\Delta t_N = \varepsilon_N \Delta g_N \ , \tag{52}$$

$$\Delta t^{trial}_{T_1} = \varepsilon_T\big[m_{11}\Delta\bar{\xi} + 2(\bar{\mathbf{x}}_{,\xi\xi}\cdot\boldsymbol{\tau}_1\Delta\bar{\xi}\Delta\bar{\mathbf{x}}_{,\xi}\cdot\boldsymbol{\tau}_1)(\bar{\xi} - \bar{\xi}_n)\big] \ , \tag{53}$$

$$\Delta t_{T_1} = -\mu\varepsilon_N \mathrm{sgn}(t^{trial}_{T_1})\Big[\sqrt{m_{11}}\Delta g_N + \frac{g_N}{\sqrt{m_{11}}}(\bar{\mathbf{x}}_{,\xi\xi}\cdot\boldsymbol{\tau}_1\Delta\bar{\xi} + \Delta\bar{\mathbf{x}}_{,\xi}\cdot\boldsymbol{\tau}_1)\Big] \ , \tag{54}$$

where Δg_N and $\Delta\bar{\xi}$ can be obtained by simply substituting the variational sign δ with the incremental sign Δ in (49).

The implementation details of these contact variables can be found in Appendix A.1.

3.4. Mortar-based contact algorithm

The completion of the contact algorithm relates to the computation of the contact integrals in (47) and (48). Generally, the segment-based method and element-based method are distinguished by the discretisation of the contact area. Gauss-point-to-surface (GPTS) method and mortar-based method are distinguished by the use of different integration treatments. Although segment-based discretisation provides a more accurate result, it incurs a complicated formulation and heavy computation efforts. The element-based method, on the other hand, is easy to implement, and the accuracy can be enhanced by increasing the number of integration points. Recently, a hybrid method termed boundary-segmentation method has also been proposed

which combines the merits of two integration schemes [50]. GPTS method uses Gauss quadrature points for the evaluation of contact integral, which often causes over-constrained problems leading to undesirable oscillations of contact tractions, especially at the edge of the contact area, when the penalty parameter is set to a large value. The mortar-based method is essentially a weak enforcement of the contact constraints by projecting the constraints to the control points through the integration over the local contact element. In this work, element-based method together with mortar-based algorithm is used to evaluate the contact integral. The contact virtual work is reformulated as

$$\delta W_c = \sum_A (t_{NA}\delta g_{NA} + t_{TA}\delta\bar{\xi}_A)A_A \ , \tag{55}$$

where the normal gap and the parametric projections are determined through a weighted average of their local values on the contact surface, with the NURBS basis functions as weights

$$g_{NA} = \frac{\int_{\Gamma_c} R_A \ g_N \ \mathrm{d}\Gamma}{\int_{\Gamma_c} R_A \ \mathrm{d}\Gamma} \quad \bar{\xi}_A = \frac{\int_{\Gamma_c} R_A \ \bar{\xi} \ \mathrm{d}\Gamma}{\int_{\Gamma_c} R_A \ \mathrm{d}\Gamma} \ , \tag{56}$$

where subscript A indicates the active control points, which are determined through the criteria $g_{NA} \leq 0$. $A_A = \int_{\Gamma_c} R_A \ \mathrm{d}\Gamma$ is the tributary area. The variational and incremental form of (56) can be obtained immediately via replacing the corresponding variables in the integrals by their variational or incremental form

$$\delta g_{NA} = \frac{\int_{\Gamma_c} R_A \ \delta g_N \ \mathrm{d}\Gamma}{\int_{\Gamma_c} R_A \ \mathrm{d}\Gamma} \quad \Delta g_{NA} = \frac{\int_{\Gamma_c} R_A \ \Delta g_N \ \mathrm{d}\Gamma}{\int_{\Gamma_c} R_A \ \mathrm{d}\Gamma} \quad \delta\bar{\xi}_A = \frac{\int_{\Gamma_c} R_A \ \delta\bar{\xi} \ \mathrm{d}\Gamma}{\int_{\Gamma_c} R_A \ \mathrm{d}\Gamma} \quad \Delta\bar{\xi}_A = \frac{\int_{\Gamma_c} R_A \ \Delta\bar{\xi} \ \mathrm{d}\Gamma}{\int_{\Gamma_c} R_A \ \mathrm{d}\Gamma} \ , \tag{57}$$

and the incremental variational form of these variables are as

$$\Delta\delta g_{NA} = \frac{\int_{\Gamma_c} R_A \ \Delta\delta g_N \ \mathrm{d}\Gamma}{\int_{\Gamma_c} R_A \ \mathrm{d}\Gamma} \quad \Delta\delta\bar{\xi}_A = \frac{\int_{\Gamma_c} R_A \ \Delta\delta\bar{\xi} \ \mathrm{d}\Gamma}{\int_{\Gamma_c} R_A \ \mathrm{d}\Gamma}. \tag{58}$$

Additionally, the mortar treatment of the metric and its linearisation results in

$$m_{11A} = \frac{\int_{\Gamma_c} R_A \ m_{11} \ \mathrm{d}\Gamma}{\int_{\Gamma_c} R_A \ \mathrm{d}\Gamma} \quad \Delta m_{11A} = \frac{\int_{\Gamma_c} R_A \ \Delta m_{11} \ \mathrm{d}\Gamma}{\int_{\Gamma_c} R_A \ \mathrm{d}\Gamma}. \tag{59}$$

The contact traction in the normal direction with its incremental form as a result of projection to control points becomes

$$t_{NA} = \varepsilon_N g_{NA} \quad \Delta t_{NA} = \varepsilon_N \Delta g_{NA} \ , \tag{60}$$

and in the tangential direction

$$t_{TA} = \begin{cases} t_{TA}^{\mathrm{trial}} = t_{TAn} + \varepsilon_T m_{11A}(\bar{\xi}_A - \bar{\xi}_{An}) & \text{if } \|\mathbf{t}_{TA}^{\mathrm{trial}}\| \leq \mu|t_{NA}| \\ \mu|t_{NA}|\frac{t_{TA}^{\mathrm{trial}}}{\|\mathbf{t}_{TA}^{\mathrm{trial}}\|} = -\mu\varepsilon_N g_{NA}\frac{t_{TA}^{\mathrm{trial}}}{\|\mathbf{t}_{TA}^{\mathrm{trial}}\|} & \text{otherwise.} \end{cases} \tag{61}$$

$$\Delta t_{TA} = \begin{cases} \Delta t_{TA}^{\mathrm{trial}} = t_{TAn} + \varepsilon_T \Delta m_{11A}(\bar{\xi}_A - \Delta\bar{\xi}_{An}) & \text{if } \|\mathbf{t}_{TA}^{\mathrm{trial}}\| \leq \mu|t_{NA}| \\ -\mu\varepsilon_N \mathrm{sgn}(t_{TA}^{\mathrm{trial}})\Big[\sqrt{m_{11A}}\Delta g_{NA} + \frac{g_{NA}}{2\sqrt{m_{11A}}}\Delta m_{11A}\Big] & \text{otherwise.} \end{cases} \tag{62}$$

Finally, the residual term and the tangent stiffness matrix need to be derived for the contact algorithm. Substitute (57), (60) and (61) into (55), we have

$$\begin{aligned}\delta W_c &= \sum_A \Big(\varepsilon_N g_{NA} \int_{\Gamma_c} R_A \delta g_N \mathrm{d}\Gamma + t_{TA} \int_{\Gamma_c} R_A \delta\bar{\xi} \mathrm{d}\Gamma\Big) \\ &= \int_{\Gamma_c} \Big[\Big(\varepsilon_N \sum_A g_{NA} R_A\Big)\delta g_N + \Big(\sum_A t_{TA} R_A\Big)\delta\bar{\xi}\Big] \mathrm{d}\Gamma \ ,\end{aligned} \tag{63}$$

The linearisation of (55) comprises two parts, namely, the 'main' component and the 'geometric' component as

$$\Delta\delta W_c = \Delta\delta W_{c,m} + \Delta\delta W_{c,g} \ , \tag{64}$$

where

$$\begin{aligned}\Delta\delta W_{c,m} &= \sum_A t_{NA}(\delta g_{NA} + \Delta t_{TA}\delta\bar{\xi}_A)A_A \\ &= \sum_A \varepsilon_N \Delta g_{NA}\delta g_{NA} A_A + \sum_{A,\text{stick}} \Delta t_{TA}^{\text{stick}} \delta\bar{\xi}_A A_A + \sum_{A,\text{slip}} \Delta t_{TA}^{\text{slip}} \delta\bar{\xi}_A A_A \\ &= \sum_A \Big(\frac{\varepsilon_N}{\int_{\Gamma_c} R_A \,\mathrm{d}\Gamma} \int_{\Gamma_c} R_A \delta g_N \,\mathrm{d}\Gamma \int_{\Gamma_c} R_A \Delta g_N \,\mathrm{d}\Gamma\Big) \\ &+ \sum_{A,\text{stick}} \Delta t_{TA}^{\text{stick}} \int_{\Gamma_c} R_A \delta\bar{\xi} \,\mathrm{d}\Gamma + \sum_{A,\text{slip}} \Delta t_{TA}^{\text{slip}} \int_{\Gamma_c} R_A \delta\bar{\xi} \,\mathrm{d}\Gamma\end{aligned} \tag{65}$$

and

$$\begin{aligned}\Delta\delta W_{c,g} &= \sum_A (t_{NA}\Delta\delta g_{NA} + t_{TA}\Delta\delta\bar{\xi}_A)A_A \\ &= \sum_A \Big(\varepsilon_N g_{NA} \int_{\Gamma_c} R_A \Delta\delta g_N \,\mathrm{d}\Gamma + t_{TA} \int_{\Gamma_c} R_A \Delta\delta\bar{\xi} \,\mathrm{d}\Gamma\Big) \\ &= \int_{\Gamma_c} \Big[\Big(\varepsilon_N \sum_A g_{NA} R_A\Big)\Delta\delta g_N + \Big(\sum_A t_{TA} R_A\Big)\Delta\delta\bar{\xi}\Big] \,\mathrm{d}\Gamma.\end{aligned} \tag{66}$$

The implementation details for the tangent stiffness matrix can be found in Appendix A.2.

3.5. Validation case: Hertzian contact problem

The classical Hertzian frictional contact problem is investigated to validate the contact algorithm developed above. The basic setting of the Hertzian contact problem is depicted in Fig.6, in which a quarter of a cylinder with a radius $R = 1$ [m] is pressed under a uniform vertical traction $p_y = 10^{-3}$ [Pa] to a rigid plane. The horizontal displacements of the nodes on the left side of the cylinder are fixed to zero due to the symmetrical condition. The coefficient of friction is set as $\mu = 0.7$. The material of the cylinder is linearly elastic with Young's module $E = 1$ [Pa] and Poisson ratio $\nu = 0.3$. To capture this small deformation, the geometry is locally refined such that 70% of the mesh is condensed in 5% of the geometry close to the contact region, as shown in Fig.6. The resulting normal and tangential contact tractions are normalised by the magnitude of normal contact force of the analytical solution of the frictionless contact problem, which is written as [51]

$$p = \frac{4Rp_y}{\pi a}\sqrt{a^2 - x^2}, \quad a = 2\sqrt{\frac{2R^2 p_y(1-\nu^2)}{E\pi}}. \tag{67}$$

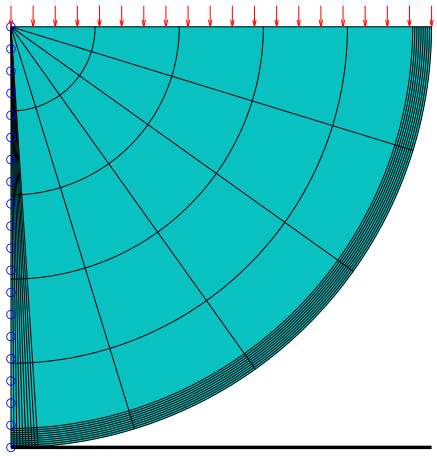

Fig. 6. Basic setting of Hertzian contact problem

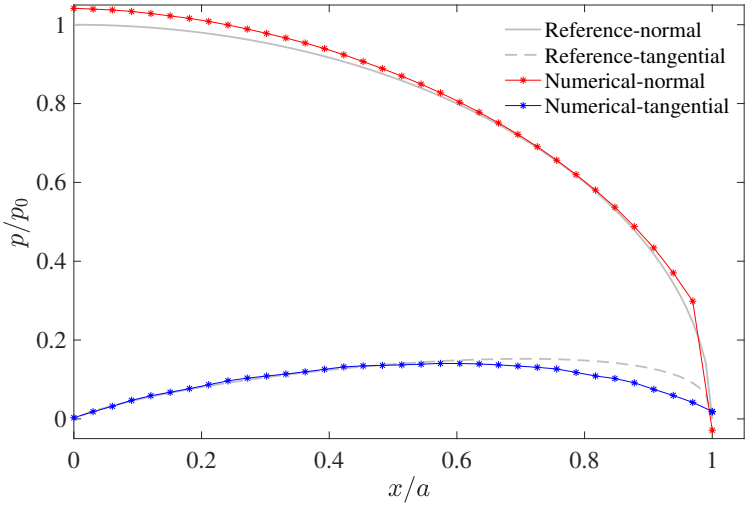

Fig. 7. Normalised results of normal and tangential contact tractions

It has been explained in detail in [17] that the applied load needs to be small enough for the small deformation assumption underlying equation (67) to hold. Since the closed-form solution of the tangential contact traction is not available in the literature, a semi-analytical solution is used instead, which is based on the uncoupling assumption of the normal and tangential contact stress. The normalised contact tractions against normalised coordinates (x/a) for both the reference and numerical results are depicted in Fig.7. Due to the uncoupling assumption used in deriving the tangential contact force and the normal contact force being taken from frictionless contact result, some discrepencies among the analytical and numerical results are expected. Nevertheless, they are generally in good consistency, thus proving the efficiency of the contact algorithm. The authors would like to note that other contact algorithm, e.g. GPTS based contact algorithms [19, 20], may not get such good consistency, especially at the edge (e.g. $x/a \sim 1$), where tremendous oscillations may occur due to the over-constraint nature of those algorithms and a post-processing procedure is often required to alleviate the oscillations in the results.

4. Contact analysis of 2D randomly rough surfaces

In this section, the random geometry modelling method presented in Sec.2 and the contact algorithm developed hereinbefore are combined to construct an extended method for contact problems involving randomly rough surfaces. To demonstrate this method, the contact between 2D randomly rough surfaces will be analysed. In the two-dimensional setting, random surfaces degenerate into 1D random profiles, which can usually be characterised by spatial property as Root Mean Square (RMS) roughness and spectral property as correlation length. The problem is set to be on a mesoscopic scale, that is to say, from micrometre (μm) to millimetre (mm) for our examples of interests. The main objective of the contact analysis is to see how the local COF relates to the global COF under the condition of unilateral or bilateral rough contact. For unilateral roughness condition, a prescribed roughness is imposed to either the elastic body or the rigid

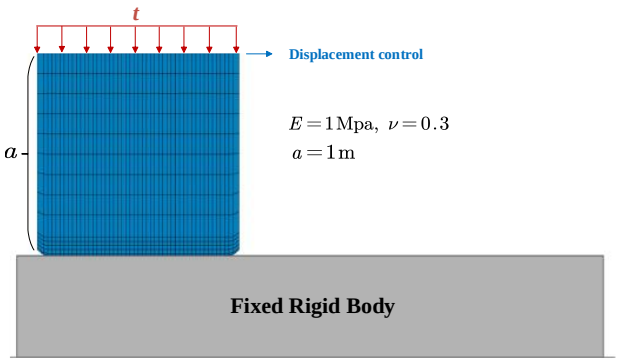

Fig. 8. Baseline model

body (termed 'rough' in the following), while the other side in contact is considered to have a significantly lower level of roughness (termed 'smooth' in the following) in the initial configuration. When the contact occurs, the elastomer will be forced to deform while the rigid body exhibits no deformation during the whole process. For bilateral roughness condition, random roughness of the same level is imposed to both surfaces before contact. The second objective is to analyse the development of the real contact area, which is usually only part of the nominal contact area, as the parameters such as the roughness change. It should be noted that the investigations in this work merely demonstrate the capacity of the analysis framework to establish the link between local COF and global COF in computational aspect, rather than reflecting the complicated physical mechanism of the frictional contact phenomena. In this case, only elastic contact is of concern and plastic and thermal effects are excluded and thus friction is the sole source of energy dissipation.

4.1. Baseline model

A baseline model, shown in Fig.8, is introduced for illustrating the procedures of the numerical experiments to be presented. A square-shaped elastomer (slave body) with length $a = 1$ [m] contacts against a fixed rigid body (master body) under a uniform normal pressure t at the top of the elastomer. The material of the elastomer is modelled by the Neo-Hookean model with Young's modulus $E = 1$ [MPa] and Poisson's ratio $\nu = 0.3$. The elastomer is discretised by cubic NURBS basis functions and is further refined near the contact interface, where the mesh size h is required to be smaller than the minimum correlation lengths of rough surfaces from either side of the contact interface. Here the mesh size is typically set as $h = 0.5 \min\{\tilde{l}_s, \tilde{l}_m\}$, where $\tilde{l}_s$ and $\tilde{l}_m$ are respectively the smallest correlation lengths of the slave and master surfaces. The normal traction t is loaded through an incremental approach to ensure convergence of the algorithm. When the normal loading is applied, the traction boundary condition employed to the nodes of the top mesh is converted to displacement boundary condition by fixing their vertical displacements at this instant. This conversion is introduced to prevent the elastomer from toppling down when meeting with kinks from the randomly rough surface of the rigid body. For the same reason, the control points in the left and right corners of the bottom side of the elastomer are lifted slightly about $0.01a$. Afterwards, a displacement control in the horizontal direction is employed to the nodes at the top edge of the elastomer to trigger the

frictional sliding process and last for a long enough length. The local COF is set as $\mu_o = 0.2$. The global COF, however, needs to be calculated with the integration of normal and tangential (with respect to the moving direction) forces at the interface, as

$$\mathbf{F}_N = \int_{\Gamma_c} \varepsilon_N |\langle \sum_A g_{NA} R_A \rangle_-| \cdot \mathbf{n} \, \mathrm{d}\Gamma = [F_{Nx}, F_{Ny}]^{\mathrm{T}}, \tag{68}$$

$$\mathbf{F}_T = \int_{\Gamma_c} \sum_A t_{TA} R_A \cdot \boldsymbol{\tau}^1 \, \mathrm{d}\Gamma = [F_{Tx}, F_{Ty}]^{\mathrm{T}}, \tag{69}$$

where $\mathbf{n}$ and $\boldsymbol{\tau}^1$ are normalised normal vector and contravariant vector of the master surface, respectively and $\langle \bullet \rangle_-$ denotes taking the negative part as shown in (43). The penalty parameters are set as $\varepsilon_N = 100E/a$ and $\varepsilon_T = 10E/a$. The instant global COF is defined as the ratio of global normal force to the global tangential force as

$$\mu_{\mathrm{ins}} = \frac{|F_{Nx} + F_{Tx}|}{|F_{Ny} + F_{Ty}|} \tag{70}$$

It is foreseeable that the instant global COF μ_{ins} would experience oscillations during the sliding process when there exists roughness. Therefore, the global COF is better quantified by taking a time average of its instant values, excluding the time of precursor to full sliding t_{pre} and lasting for a long-enough time duration T for saturation to a limit as

$$\bar{\mu}^t = \frac{1}{T} \int_{t_{\mathrm{pre}}}^{t_{\mathrm{pre}}+T} \mu_{\mathrm{ins}} \, \mathrm{d}t \tag{71}$$

The precursor to full sliding describes the transition from the initial phase after vertical loading to the full sliding phase during the frictional interaction of the elastomer with the rigid substrate. For instance, Fig.9 depicts the progress of the instant global COF with the normalised horizontal loading time. The simulation is based on "rough-smooth" setting in which a roughness of $\mathrm{RMS_s}/a = 0.001$, correlation structure as (23) and a correlation length ratio $l_s/a = 0.1$ are employed to the slave surface, while the master surface is smooth ($\mathrm{RMS_m/a} = 10^{-6}$). The normal pressure is set as $t/E = 0.01$. It is observed from Fig.9 that at the initial phase the global tangential force nearly vanishes thus the instantaneous global COF is close to zero; in the transition phase precursor to sliding, micro-slips occur and gradually accumulate and finally lead to the full sliding phase. The authors note that by saying "full sliding" they do not mean every point of the slave surface is at the state of sliding, which should be determined by the criteria described in (61) and (62), but the elastomer starts to slide as a whole such that the friction front has propagated to the entire contact interface. To illustrate this propagation, we investigated normal and tangential traction distribution of the contact interface at these two phases, as shown in Fig.10. At the initial phase (shown in Fig.10(a)), the tangential traction has both positive and negative values along the contact interface, meaning that the points on the slave surface of the elastomer have opposite moving trend approximately divided by the mid-point of the slave surface. At the full sliding phase (shown in Fig.10(b)), however, the tangential traction has only negative values and besides, the normal (tangential) traction show apparent larger values on the right side of

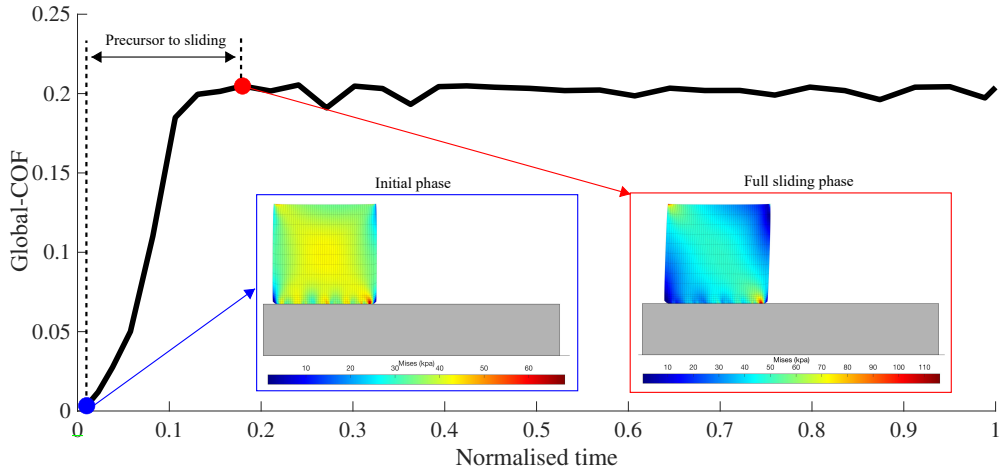

Fig. 9. Progress of the instantaneous global COF

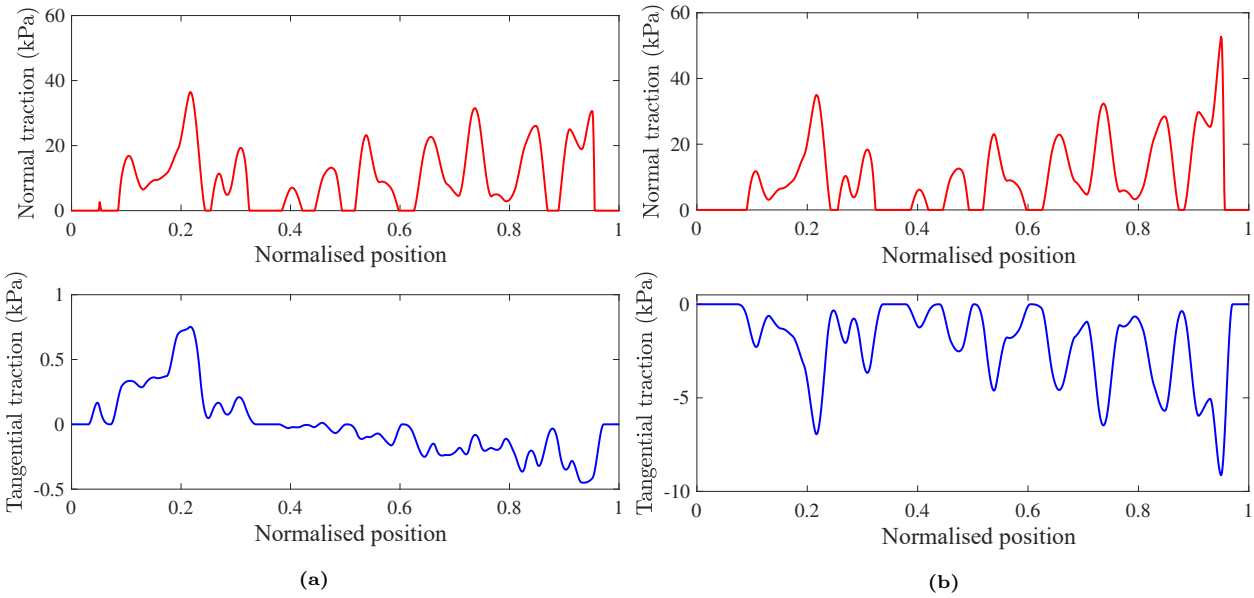

Fig. 10. Normal and tangential traction distribution of contact interface at (a) initial phase; (b) full sliding phase.

the contact interface than the left side compared to the initial phase, so that all points of the contact interface have been rearranged to show the same moving trend. During the full sliding phase, stress concentration may occur locally in the contact interface due to the employment of roughness to the slave surface, resulting in the fluctuations of the global COF, which then becomes a random variable. For representativeness, $N_s = 50$ realisations will be performed in the following investigations, and the time-averaged global COF is further quantified by the ensemble average procedure as

$$\bar{\mu} = \frac{1}{N_s} \sum_{i=1}^{N_s} \bar{\mu}_i^t \,, \tag{72}$$

where $\bar{\mu}_i^t$ indicates the i-th realisation of the time-averaged global COF. Another variable of interest is the

true contact area A_{true}. It is well-known that the area in real contact is generally smaller than the nominal contact area A_{nor}. The instantaneous ratio $(A_{\text{true}}/A_{\text{nor}})$ can be derived from the manipulation of the gap results as

$$\left(\frac{A_{\text{true}}}{A_{\text{nor}}}\right)_{\text{ins}} = \frac{1}{a}\int_{\Gamma_c} \text{sgn}(|\langle \sum_A g_{NA} R_A \rangle_-|)\text{d}\Gamma\,, \tag{73}$$

and its time-average value is expressed as

$$\left(\frac{\bar{A}_{\text{true}}}{A_{\text{nor}}}\right)^t = \frac{1}{T}\int_{t_{\text{pre}}}^{t_{\text{pre}}+T} \left(\frac{A_{\text{true}}}{A_{\text{nor}}}\right)_{\text{ins}} \text{d}t. \tag{74}$$

Finally, taking the average of N_s samples the ratio of true contact area becomes

$$\frac{\bar{A}_{\text{true}}}{A_{\text{nor}}} = \frac{1}{N_s}\sum_{i=1}^{N_s}\left(\frac{\bar{A}_{\text{true}}}{A_{\text{nor}}}\right)_i^t. \tag{75}$$

4.2. Rough-smooth contact

In the numerical experiments of 'rough-smooth' contact, the slave surface is randomly rough while the master surface is smooth. The basic parameters used in all simulations are the same as the baseline model introduced in Sec.4.1 except for the particular parameter under investigation. Fig.11(a)(c)(e) summarises a series of three investigations towards averaged macro-to-meso COF ratio $\bar{\mu}/\mu_o$ with respect to the variation of the specific simulation parameter. The dashed line in the figure indicates the result of 'smooth-smooth' case, which is a limit case when $l_s/a \to \infty$, the corresponding value of the COF is denoted by 'ssCOF' and the corresponding value of the true contact area is denoted by 'ssTCA'. First, the correlation length of the slave surface ratio l_s/a is varied, and it is observed that both the mean value and the standard deviation of $\bar{\mu}/\mu_o$ shrink with the increase of l_s/a and the mean value converges to the ssCOF as l_s/a approaches 10. The result implies that with the growth of the correlation length, the roughness of the slave surface tends to exhibit only in the global sense and the surface can be deemed as smooth in the local sense so that the global COF approaches the ssCOF. On the other hand, the global COF can remarkably deviate from the ssCOF when the correlation length is small, as the roughness becomes significantly locally fluctuant. The authors would like to point out that no homogenisation effect, which means a convergent trend of $\bar{\mu}/\mu_o$ when l_s/a becomes small, is observed in the length scale under analysis. Second, the roughness of the slave surface is varied and it is observed that $\bar{\mu}/\mu_o$ has similar mean values approaching ssCOF and small deviations when the level of roughness $\text{RMS}_s/a \in [10^{-6}, 10^{-4}]$. However, the roughness at the micrometre level will have a significant impact on both the mean value and the standard deviation of $\bar{\mu}/\mu_o$ and this justifies the choice of $\text{RMS}_s/a = 0.001$ in the baseline model. In the third case, the variation of normal pressure to elasticity ratio t/E is investigated and a continuous descending trend of $\bar{\mu}/\mu_o$ with the increase of t/E is obtained. The result suggests that the global COF is approaching or even slightly lower than the ssCOF when the normal pressure approaches $0.1E$. The authors note that this result shows a qualitatively same trend as the experimental results presented in [52], where the COF drops clearly with the increase of external pressure.

As a complementary set to the above investigations, Fig.11(b)(d)(f) summarises the results with respect to the ratio of the true contact area $\bar{A}_{\text{true}}/A_{\text{nor}}$. It is observed that as the ratio l_s/a increases, the ratio

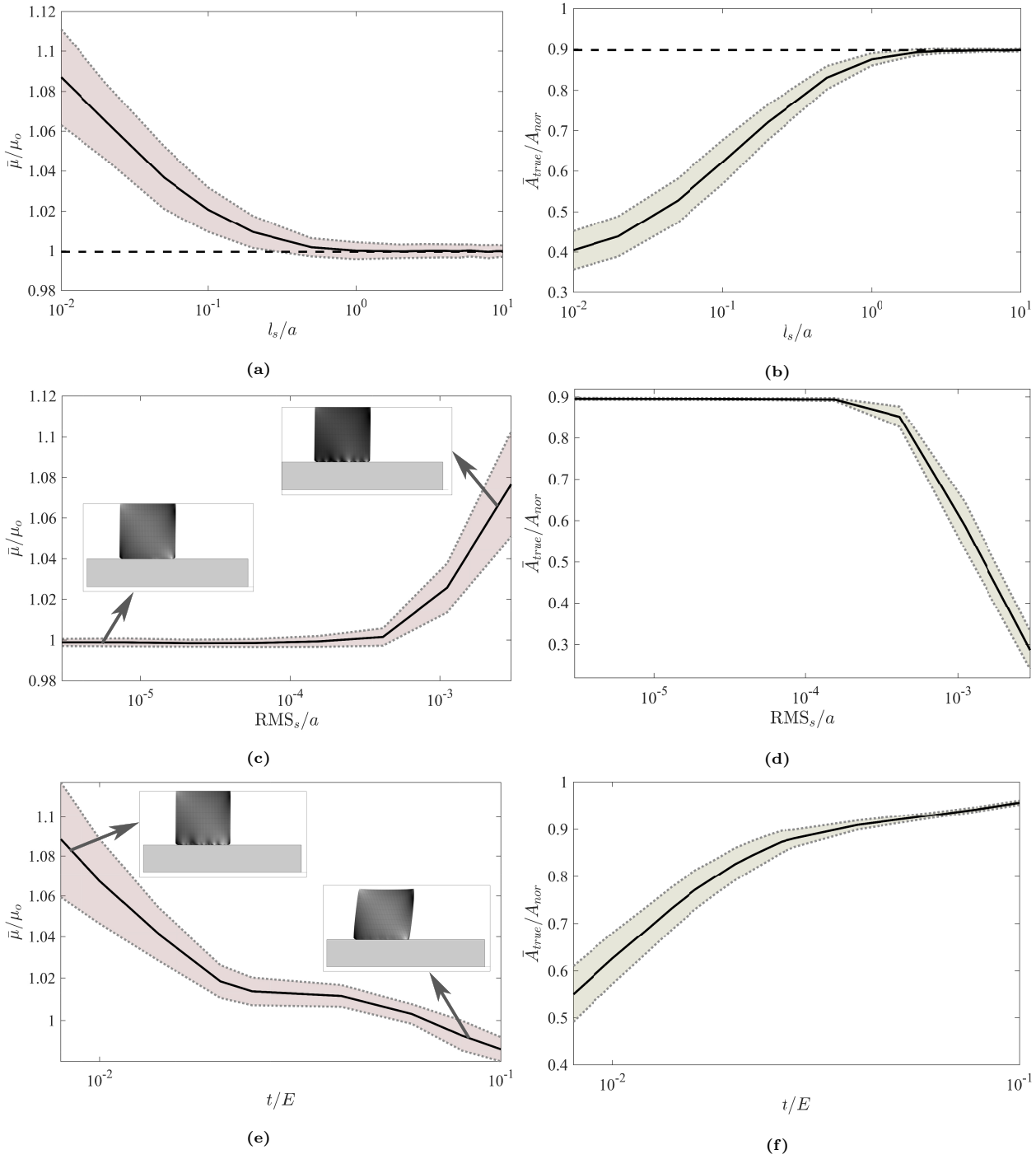

Fig. 11. Statistical results in rought-smooth contact numerical experiments of $\bar{\mu}/\mu_o$ and of $\bar{A}_{\mathrm{true}}/A_{\mathrm{nor}}$ with variation of parameters (a)(b) correlation length of slave surface ratio (l_s/a); (c)(d) roughness of slave surface ratio (RMS_s/a); (e)(f) normal pressure ratio (t/E), solid line indicates the mean values and shaded area indicate the standard deviations.

$\bar{A}_{\mathrm{true}}/A_{\mathrm{nor}}$ gradually saturates and converges at around the ssTCA with continuous decreasing standard deviations. Secondly, the micrometre-level roughness has a significant influence on the true contact area as more voids will be created when the slave surface has heavier spatial fluctuations. Finally, the true

contact area increases drastically as normal pressure grows, because the voids will be filled up by the heavily deformed elastomer body.

A further insight can be drawn from the results of Fig.11 as we collect the data of $\bar{A}_{\text{true}}/A_{\text{nor}}$ and $\bar{\mu}/\mu_o$ in all three cases and make an scatter plot, as shown in Fig.12. These results, although extracted from different settings, exhibit very similar patterns that the increase of $\bar{A}_{\text{true}}/A_{\text{nor}}$ affects negatively $\bar{\mu}/\mu_o$. These results reveals that all settings may have impacts on $\bar{\mu}/\mu_o$ through varying $\bar{A}_{\text{true}}/A_{\text{nor}}$. Indeed, when the true contact area approaches the nominal contact area, it is reasonable to deem that the global COF approaches the ssCOF since almost no singular local behaviour occurs.

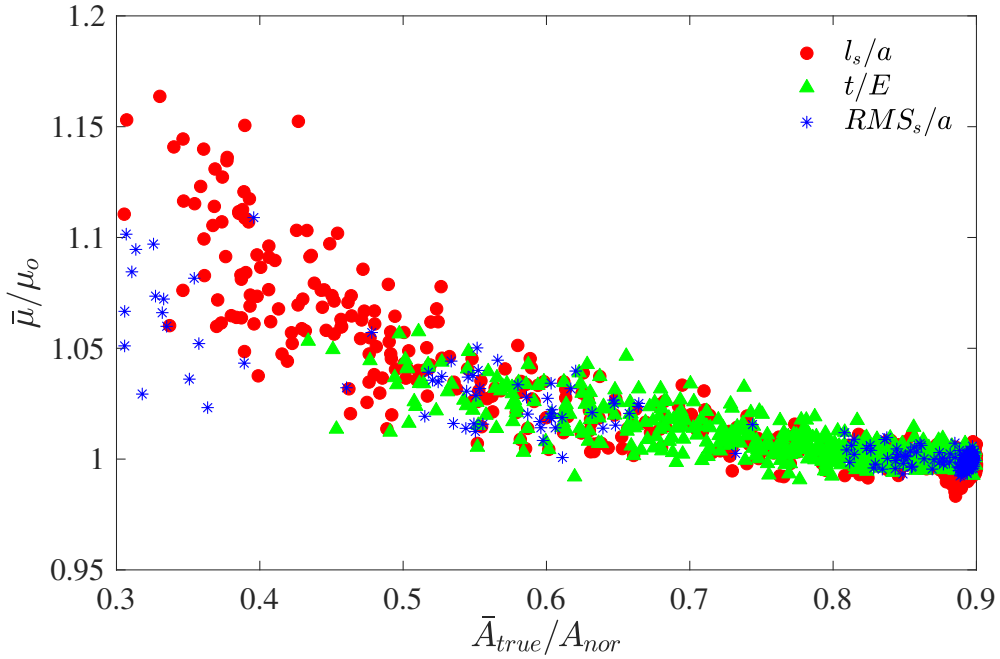

Fig. 12. Scatter plot of $\bar{\mu}/\mu_o$ with respect to $\bar{A}_{\text{true}}/A_{\text{nor}}$ by simulation results extracted from three cases in 'rough-smooth' setting.

4.3. Smooth-rough contact

The smooth-rough contact scenarios are investigated in this section by attributing roughness to the master surface only. The slave surface, though smooth at the initial configuration, is expected to deform according to the contact interface when applied with contact forces. The global COF is more likely to fluctuate because of the variation of the contact angle [36], which describes the angle between the direction of local contact forces and the global motion, along the contact interface.

The parametric analyses with respect to $\bar{\mu}/\mu_o$ and $\bar{A}_{\text{true}}/A_{\text{nor}}$ are shown in Fig.13(a)(c)(e) and Fig.13(b)(d)(f), respectively. In an overview of the results, the global COF is found to be less than the ssCOF (indicated again by the dashed line) in most of the cases, in contrast with the 'rough-smooth' case, indicating that the employment of roughness to the rigid contact surface will result in the decrease of global COF with respect

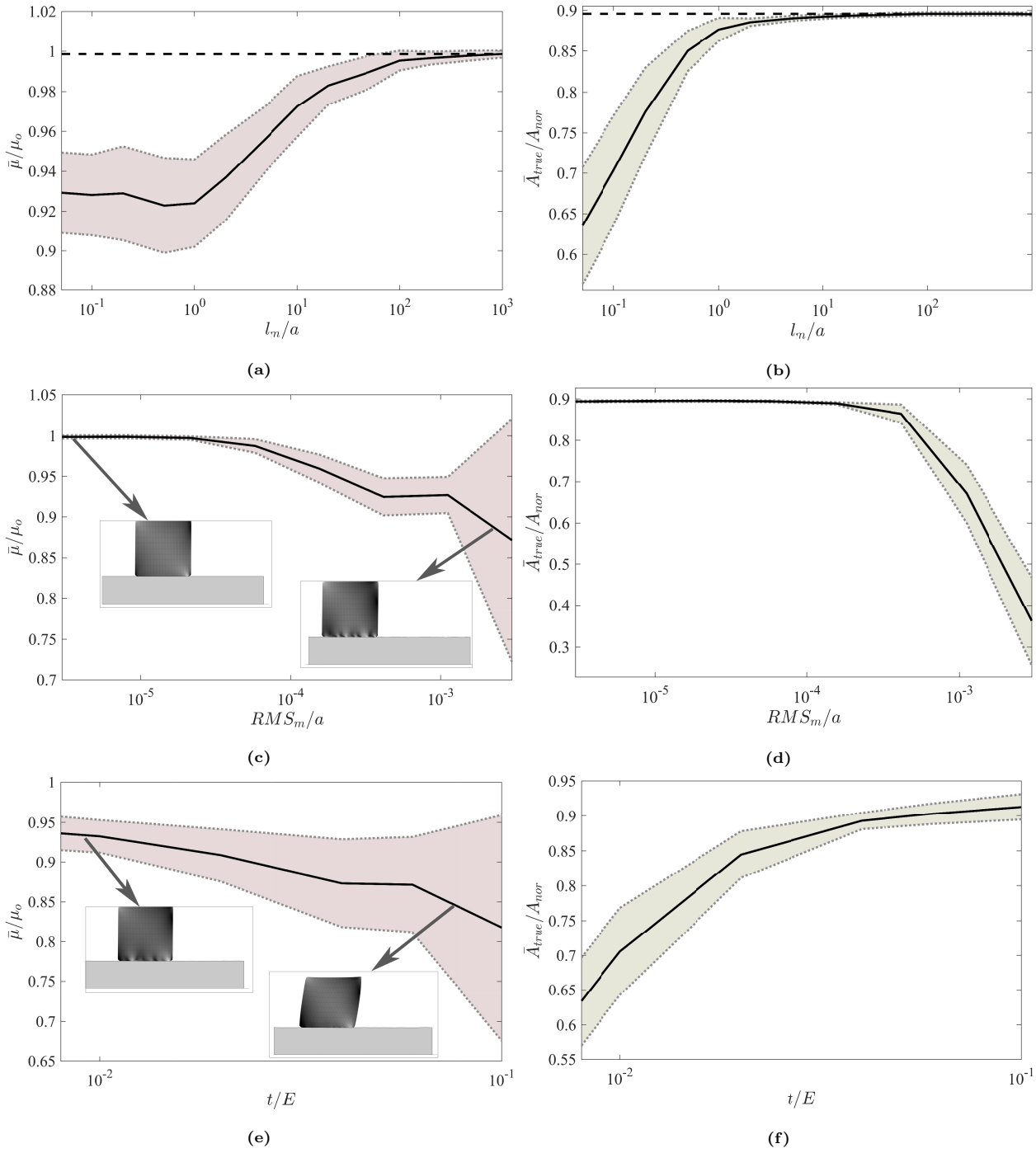

Fig. 13. Statistical results in smooth-rough contact numerical experiments of $\bar{\mu}/\mu_o$ and $\bar{A}_{\text{true}}/A_{\text{nor}}$ with variation of parameters (a)(b) correlation length of master surface ratio (l_m/a); (c)(d) roughness of master surface ratio (RMS_m/a); (e)(f) normal pressure ratio (t/E), solid line indicates the mean values and shaded area indicate the standard deviations.

to the ssCOF. The results related to $\bar{A}_{\text{true}}/A_{\text{nor}}$ are similar to the 'rough-smooth' scenario. As for individual parameters, firstly, the effect of the correlation length of the master surface (l_m) is not monotonic as the global COF decreases when $l_m/a < 1$ and increases asymptotically to the ssCOF when $l_m/a > 1$. Secondly,

the roughness of the master surface on the scale of 10^{-4} has a significant influence on the global COF. The global COF has in general a decreasing trend with the growth of roughness, in contrast to the 'rough-smooth' case where the trend is the opposite. Finally, the increase of normal pressure causes the decrease of $\bar{\mu}/\mu_o$ but the increase of the standard deviation.

4.4. Rough-rough contact

The last numerical experiment is conducted under the condition of the 'rough-rough' contact setting, in which $\mathrm{RMS}_s/a = \mathrm{RMS}_m/a = 0.001$ is used. The 'rough-rough' contact setting is the most commonly seen case in reality and the effects of the reported 'rough-smooth' and 'smooth-rough' cases are expected to be combined. The variations of $\bar{\mu}/\mu_o$ and $\bar{A}_{\mathrm{true}}/A_{\mathrm{nor}}$ is firstly investigated concerning the variations of both the correlation length of the slave surface to size ratio l_s/a and the correlation length of the master surface to size ratio l_m/a, as depicted in Fig.14. The results reveal the distinct impacts of l_s/a and l_m/a on $\bar{\mu}/\mu_o$: it increases with the growth of l_m/a but decreases with the growth of l_s/a, which means that a smoother elastic surface will result in a lower global COF, whereas a smoother rigid surface will lead to a higher one. The true contact area ratio $\bar{A}_{\mathrm{true}}/A_{\mathrm{nor}}$, as expected, increases with either the growth of l_s/a or l_m/a, indicating a smoother slave or master surface will lead to a larger true contact area.

Fig.15(a) and Fig.15(b) illustrate the numerical experimental results concerning the normal pressure ratio t/E. It can be observed that an increasing normal pressure results in the decreasing of the global COF with increasing standard deviations and also in the increasing of the true contact area with shrinking standard deviations. These results are again in consistence with those of the last two numerical experimental scenarios. The results of varying RMS of both surfaces are not shown here, as the simulations are highly sensitive to the roughness and often encounter difficulties in convergence when both surfaces possess a high RMS.

As a comparison among three different settings, the mean values of $\bar{\mu}/\mu_o$ and $\bar{A}_{\mathrm{true}}/A_{\mathrm{nor}}$ with variation of normal pressure ratio t/E are exhibited in Fig.16. For the global/local COF ratio, one can observe distinct patterns in these cases whether the rigid surface is imposed a certain level of roughness or not. Generally, a rough rigid surface will result in the decrease of the global/local COF ratio, which is due to the multi-directional distributions of local normal and tangential forces. On the other side, a smoother surface of either side can lead to the increase of the true contact ratio, while the difference is only significant when a small external force is applied.

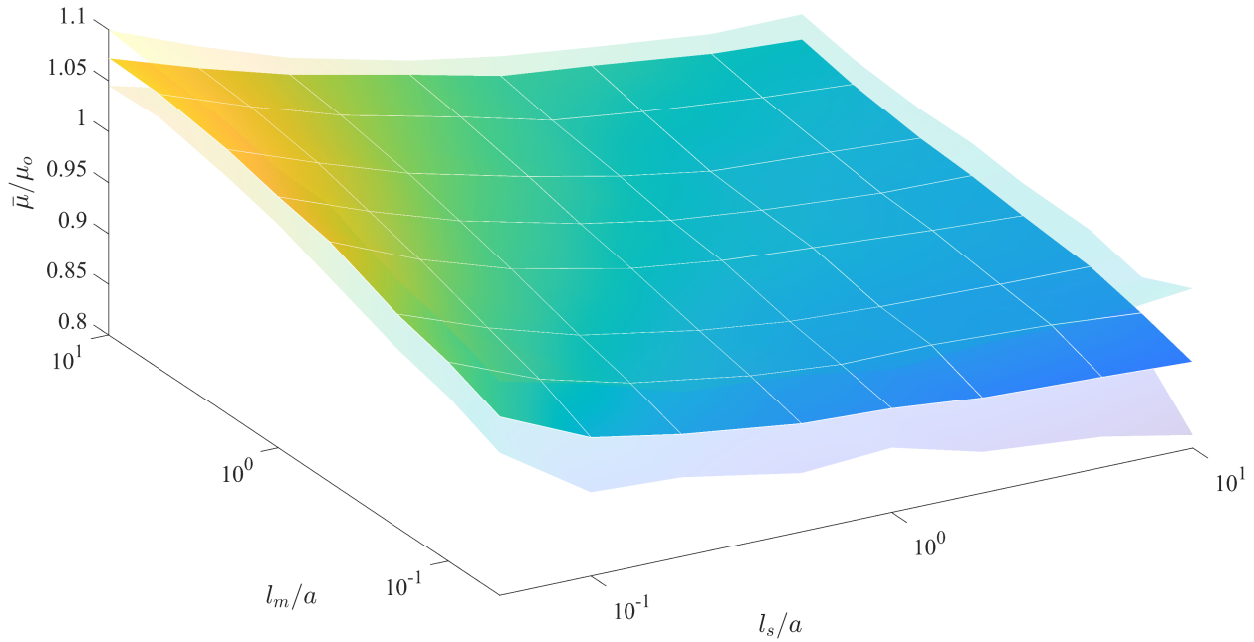

(a)

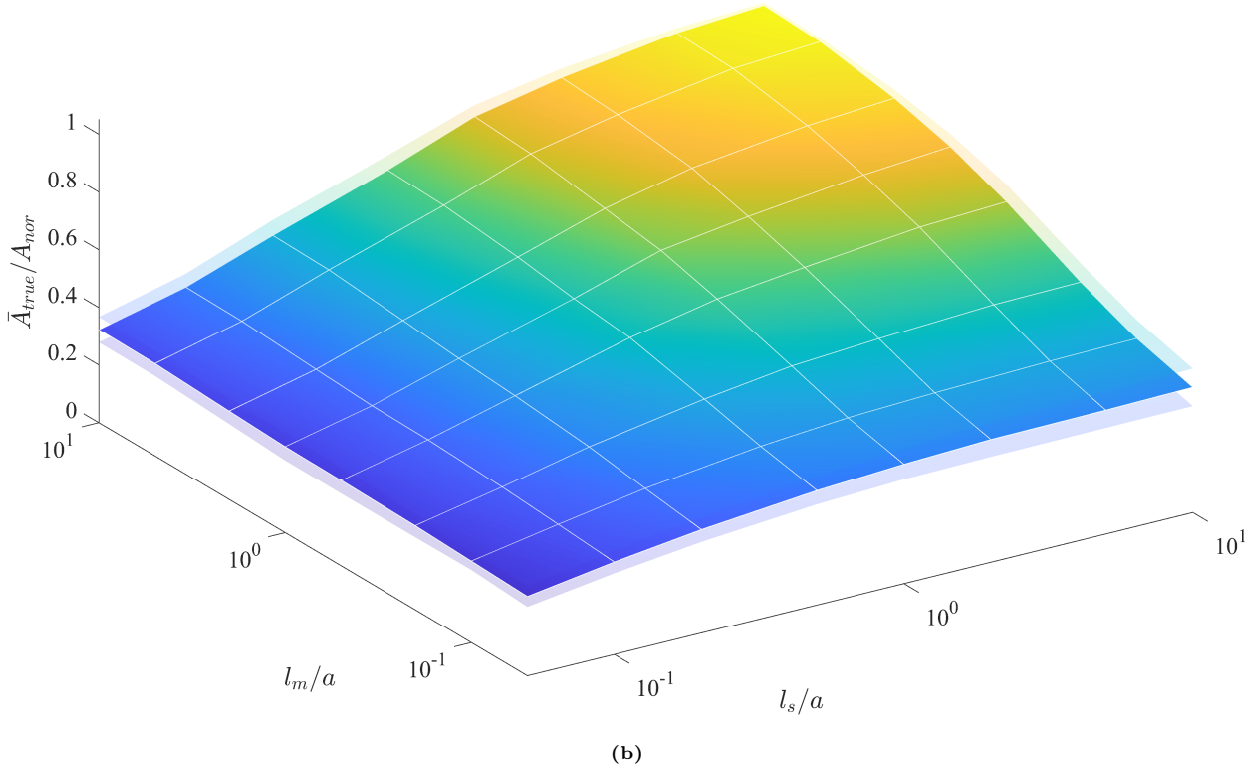

(b)

Fig. 14. Statistical results in rough-rough contact numerical experiments of (a) $\bar{\mu}/\mu_o$; (b) $\bar{A}_{\mathrm{true}}/A_{\mathrm{nor}}$ with variation of correlation length of slave surface ratio (l_s/a) and master surface ratio (l_m/a), entity plot indicates the mean value and shaded plot indicates the standard deviation.

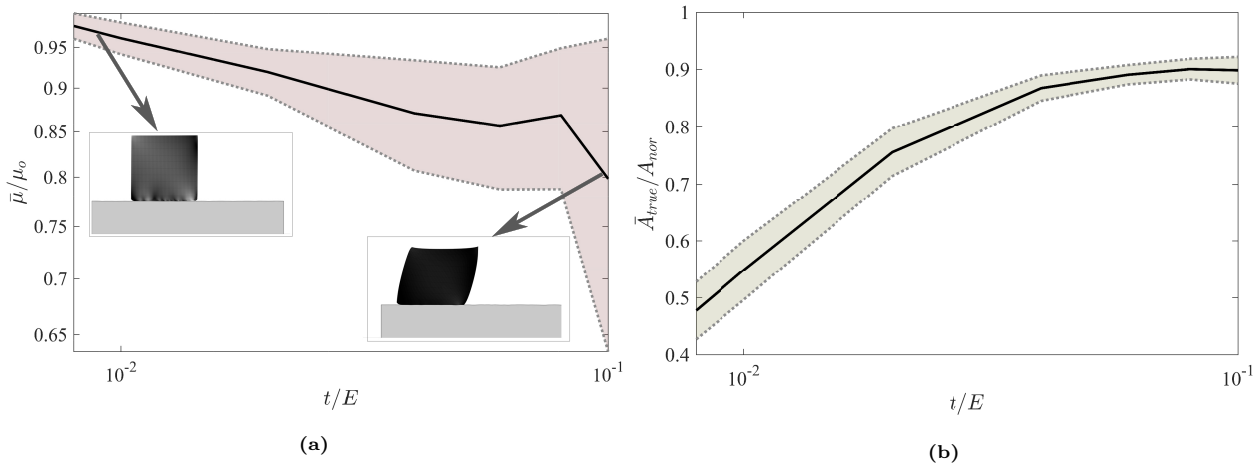

Fig. 15. Statistical results in rough-rough contact numerical experiments of (a) $\bar{\mu}/\mu_o$ and (b) $\bar{A}_{\text{true}}/A_{\text{nor}}$ with variation of normal pressure ratio (t/E), solid line indicates the mean values and shaded area indicate the standard deviations.

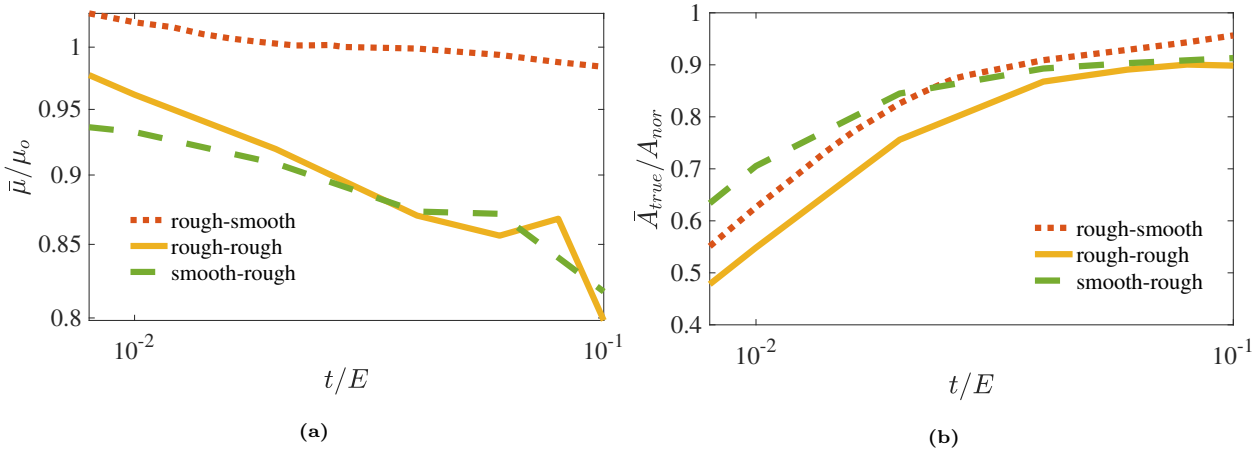

Fig. 16. Comparison of the mean values under different settings for (a) $\bar{\mu}/\mu_o$ and (b) $\bar{A}_{\text{true}}/A_{\text{nor}}$ with variation of normal pressure ratio (t/E)

5. Conclusions

In this paper, a new Isogeometric analysis based method for frictional contact analysis has been presented. This method is based on two ingredients. Firstly, an Isogeometric random geometry modelling framework was proposed to facilitate the implementation of a randomly rough surface to a precisely described geometry, which made use of random field modelling with the K-L expansion method and Non-Uniform Rational B-Spline (NURBS) curve and interpolation method. The second ingredient concerned a robust and accurate contact algorithm targeting frictional contact problems. To this end, a mortar-based variational formulation of contact mechanics with contact constraints enforced by the penalty method was developed by incorporating a new closest projection point search algorithm.

The results presented in this paper are focused on the determination of the global coefficient of friction (COF) and true contact area of the randomly rough contact interface between an elastomer and a rigid body with prescribed local COF in the 2D large deformation regime. Numerical experiments were performed in three different settings regarding which side of the contacting bodies was attributed with a randomly rough surface, namely 'rough-smooth', 'smooth-rough' and 'rough-rough' contact conditions. The statistical properties of the effective global COF and true contact area were characterised by the Monte-Carlo sampling for multiple realisations. Overall, it was found that correlation length and RMS of the random surface roughness and the external normal pressure were of significant importance to the global COF and true contact area. Moreover, the global COF was generally above the 'smooth-smooth' case one when the roughness was employed only to the contact surface of elastomer, while it was below the 'smooth-smooth' case one when only the rigid body surface is rough. Finally, it is observed that the global COF was mainly impacted by the true contact area with a decreasing trend in the 'rough-smooth' case.

Acknowledgments

The first author H. Hu gratefully acknowledges the financial support from the University of Liverpool and China Scholarship Council Awards (CSC NO.201906230311).

Appendix A Implementation details of the contact algorithm.

A.1 Discretised representation of contact variables

In the Isogeometric framework, the NURBS basis functions introduced in Sec.2.1 play the role of the shape functions in the traditional finite element method. The contact variables of interest thus can be interpolated by using these functions, for example, the displacement and its variation on an element can be expressed as

$$\mathbf{u}^e = \sum_{I=1}^{n_e} R_I \mathbf{u}_I \quad \delta\mathbf{u}^e = \sum_{I=1}^{n_e} R_I \delta\mathbf{u}_I \ , \tag{A.1}$$

where $R_I = R^{(d_s)}_{I,\mathbf{p}}$ with the degree $\mathbf{p}$ and dimensional indicator (d_s) omitted, and n_e is the number of control points whose corresponding basis functions have supports on the element. In this case, (49) can be represented via interpolated variables as

$$\delta g_N = \Big[\sum_{I=1}^{n_e^s} R_I^s(\xi^s)\delta\mathbf{u}_I^s - \sum_{I=1}^{n_e^m} R_I^m(\bar{\xi}^m)\delta\mathbf{u}_I^m\Big]\cdot\mathbf{n}\ , \tag{A.2}$$

$$\delta\bar{\xi} = H^{11}\Big[\Big(\sum_{I=1}^{n_e^s} R_I^s(\xi^s)\delta\mathbf{u}_I^s - \sum_{I=1}^{n_e^m} R_I^m(\bar{\xi}^m)\delta\mathbf{u}_I^m\Big)\cdot\boldsymbol{\tau}_1 + g_N\mathbf{n}\cdot\sum_{I=1}^{n_e^m} R_{I,\xi}^m(\bar{\xi}^m)\delta\mathbf{u}_I^m\Big]. \tag{A.3}$$

The authors would like to note that since the master body is fixed, its displacement field is a zero vector and the formulation can be simplified by dropping off the terms related to the master body. Denote $\lfloor\cdot\rfloor_s$ as the vector containing quantities related to the slave body only, for instance

$$\delta\mathbf{u} = \begin{bmatrix}\delta\mathbf{u}_1^s\\ \vdots\\ \delta\mathbf{u}_{n_e^s}^s\\ \delta\mathbf{u}_1^m\\ \vdots\\ \delta\mathbf{u}_{n_e^m}^m\end{bmatrix}\quad \Delta\mathbf{u} = \begin{bmatrix}\Delta\mathbf{u}_1^s\\ \vdots\\ \Delta\mathbf{u}_{n_e^s}^s\\ \Delta\mathbf{u}_1^m\\ \vdots\\ \Delta\mathbf{u}_{n_e^m}^m\end{bmatrix}\quad \lfloor\delta\mathbf{u}\rfloor_s = \begin{bmatrix}\delta\mathbf{u}_1^s\\ \vdots\\ \delta\mathbf{u}_{n_e^s}^s\end{bmatrix}\quad \lfloor\Delta\mathbf{u}\rfloor_s = \begin{bmatrix}\Delta\mathbf{u}_1^s\\ \vdots\\ \Delta\mathbf{u}_{n_e^s}^s\end{bmatrix} \tag{A.4}$$

The following vectors are defined in a similar manner as

$$\lfloor\mathbf{N}\rfloor_s = \begin{bmatrix}R_1^s(\xi^s)\mathbf{n}\\ \vdots\\ R_{n_e^s}^s(\xi^s)\mathbf{n}\end{bmatrix}\quad \lfloor\mathbf{T}\rfloor_s = \begin{bmatrix}R_1^s(\xi^s)\boldsymbol{\tau}_1\\ \vdots\\ R_{n_e^s}^s(\xi^s)\boldsymbol{\tau}_1\end{bmatrix} \tag{A.5}$$

$$\lfloor\mathbf{D}_1\rfloor_s = H^{11}\lfloor\mathbf{T}\rfloor_s\quad \lfloor\bar{\mathbf{N}}_1\rfloor_s = -k_{11}\lfloor\mathbf{D}_1\rfloor_s\quad \lfloor\bar{\mathbf{T}}_1\rfloor_s = -\boldsymbol{\tau}_1\cdot\bar{\mathbf{x}}^m_{,\xi\xi}\lfloor\mathbf{D}_1\rfloor_s\ , \tag{A.6}$$

such that the variation and linearisation variables discussed in the last section can be rearranged into matrix form as

$$\lfloor\delta g_N\rfloor_s = \lfloor\delta\mathbf{u}\rfloor_s^{\mathrm{T}}\lfloor\mathbf{N}\rfloor_s\quad \lfloor\delta\bar{\xi}\rfloor_s = \lfloor\delta\mathbf{u}\rfloor_s^{\mathrm{T}}\lfloor\mathbf{D}_1\rfloor_s \tag{A.7}$$

$$\lfloor\Delta g_N\rfloor_s = \lfloor\mathbf{N}\rfloor_s^{\mathrm{T}}\lfloor\Delta\mathbf{u}\rfloor_s\quad \lfloor\Delta\bar{\xi}\rfloor_s = \lfloor\mathbf{D}_1\rfloor_s^{\mathrm{T}}\lfloor\Delta\mathbf{u}\rfloor_s \tag{A.8}$$

$$\lfloor\Delta\delta g_N\rfloor_s = \lfloor\delta\mathbf{u}\rfloor_s^{\mathrm{T}}\Big[\frac{g_N}{m_{11}}\lfloor\bar{\mathbf{N}}_1\rfloor_s\lfloor\bar{\mathbf{N}}_1\rfloor_s^{\mathrm{T}} - k_{11}\lfloor\mathbf{D}_1\rfloor_s\lfloor\mathbf{D}_1\rfloor_s^{\mathrm{T}}\Big]\lfloor\Delta\mathbf{u}\rfloor_s \tag{A.9}$$

$$\begin{aligned}\lfloor\Delta\delta\bar{\xi}\rfloor_s = H^{11}\lfloor\delta\mathbf{u}\rfloor_s^{\mathrm{T}}\Big[&-(3\boldsymbol{\tau}_1\cdot\bar{\mathbf{x}}^m_{,\xi\xi} - g_N\mathbf{n}\cdot\bar{\mathbf{x}}^m_{,\xi\xi\xi})\lfloor\mathbf{D}_1\rfloor_s\lfloor\mathbf{D}_1\rfloor_s^{\mathrm{T}} - \lfloor\mathbf{N}\rfloor_s\lfloor\bar{\mathbf{N}}_1\rfloor_s^{\mathrm{T}}\\ &- \lfloor\bar{\mathbf{N}}_1\rfloor_s\lfloor\mathbf{N}\rfloor_s^{\mathrm{T}} - \frac{1}{m_{11}}(\lfloor\mathbf{T}\rfloor_s\lfloor\bar{\mathbf{T}}_1\rfloor_s^{\mathrm{T}} + \lfloor\bar{\mathbf{T}}_1\rfloor_s\lfloor\mathbf{T}\rfloor_s^{\mathrm{T}}\Big]\lfloor\Delta\mathbf{u}\rfloor_s\end{aligned} \tag{A.10}$$

A.2 Tangent stiffness matrix

Recall the contact virtual work

$$\begin{aligned}\delta W_c &= \sum_A \Big(\varepsilon_N g_{NA}\int_{\Gamma_c} R_A \delta g_N \mathrm{d}\Gamma + t_{TA}\int_{\Gamma_c} R_A \delta\bar{\xi}\mathrm{d}\Gamma\Big)\\ &= \int_{\Gamma_c}\Big[\Big(\varepsilon_N\sum_A g_{NA}R_A\Big)\delta g_N + \Big(\sum_A t_{TA}R_A\Big)\delta\bar{\xi}\Big]\mathrm{d}\Gamma.\end{aligned} \tag{A.11}$$

Its slave-body related part is

$$\begin{aligned}\lfloor\delta W_c\rfloor_s &= \int_{\Gamma_c}\Big[\Big(\varepsilon_N\sum_A g_{NA}R_A\Big)\lfloor\delta g_N\rfloor_s + \Big(\sum_A t_{TA}R_A\Big)\lfloor\delta\bar{\xi}\rfloor_s\Big]\mathrm{d}\Gamma\\ &= \lfloor\delta\mathbf{u}^T\rfloor_s\int_{\Gamma_c}\Big[\Big(\varepsilon_N\sum_A g_{NA}R_A\Big)\lfloor\mathbf{N}\rfloor_s + \Big(\sum_A t_{TA}R_A\Big)\lfloor\mathbf{D}_1\rfloor\Big]\mathrm{d}\Gamma\\ &= \lfloor\delta\mathbf{u}^T\rfloor_s\lfloor\mathbf{R}\rfloor_s\ ,\end{aligned} \tag{A.12}$$

where the residual force is obtained as

$$\lfloor\mathbf{R}\rfloor_s = \int_{\Gamma}\Big[\Big(\varepsilon_N\sum_A g_{NA}R_A\Big)\lfloor\mathbf{N}\rfloor_s + \Big(\sum_A t_{TA}R_A\Big)\lfloor\mathbf{D}_1\rfloor_s\Big]\mathrm{d}\Gamma. \tag{A.13}$$

Substituting (56)$\sim$(62) into (65) and (66) and taking their slave-body related parts, the following equations are obtained as

$$\begin{aligned}\lfloor\Delta\delta W_{c,m}\rfloor_s &= \lfloor\delta\mathbf{u}^{\mathrm{T}}\rfloor_s\lfloor\mathbf{K}_{c,m}\rfloor_s\lfloor\Delta\mathbf{u}\rfloor_s\\ \lfloor\Delta\delta W_{c,g}\rfloor_s &= \lfloor\delta\mathbf{u}^{\mathrm{T}}\rfloor_s\lfloor\mathbf{K}_{c,g}\rfloor_s\lfloor\Delta\mathbf{u}\rfloor_s\ ,\end{aligned} \tag{A.14}$$

where

$$\begin{aligned}\lfloor\mathbf{K}_{c,m}\rfloor_s = &\sum_A\Big[\frac{\varepsilon_N}{\int_{\Gamma_c}R_A\,\mathrm{d}\Gamma}\int_{\Gamma_c}R_A\lfloor\mathbf{N}\rfloor_s\,\mathrm{d}\Gamma\int_{\Gamma_c}R_A\lfloor\mathbf{N}\rfloor_s^{\mathrm{T}}\,\mathrm{d}\Gamma\Big]\\ &+\sum_{A,\text{stick}}\Big[\frac{\varepsilon_T}{\int_{\Gamma_c}R_A\,\mathrm{d}\Gamma}\int_{\Gamma_c}R_A\lfloor\mathbf{D}_1\rfloor_s\,\mathrm{d}\Gamma\int_{\Gamma_c}R_A\big[m_{11A}\lfloor\mathbf{D}_1\rfloor_s^{\mathrm{T}} - 2\lfloor\bar{\mathbf{T}}_1\rfloor_s^{\mathrm{T}}(\bar{\xi}_A-\bar{\xi}_{An})\big]\,\mathrm{d}\Gamma\Big]\\ &+\sum_{A,\text{slip}}\Big[\frac{\mu\varepsilon_N\mathrm{sign}(t_{TA}^{\text{trial}})}{\int_{\Gamma_c}R_A\,\mathrm{d}\Gamma}\int_{\Gamma_c}R_A\lfloor\mathbf{D}_1\rfloor_s\,\mathrm{d}\Gamma\int_{\Gamma_c}R_A\big(\sqrt{m_{11A}}\lfloor\mathbf{N}\rfloor_s^{\mathrm{T}}+\frac{g_{NA}}{\sqrt{m_{11A}}}\lfloor\bar{\mathbf{T}}_1\rfloor_s^{\mathrm{T}}\big)\,\mathrm{d}\Gamma\Big]\end{aligned} \tag{A.15}$$

$$\begin{aligned}\lfloor\mathbf{K}_{c,g}\rfloor_s = &\int_{\Gamma_c}\Big[\Big(\varepsilon_N\sum_A g_{NA}R_A\Big)\Big(\frac{g_N}{m_{11}}\lfloor\bar{\mathbf{N}}_1\rfloor_s\lfloor\bar{\mathbf{N}}_1\rfloor_s^T - k_{11}\lfloor\mathbf{D}_1\rfloor_s\lfloor\mathbf{D}_1\rfloor_s^{\mathrm{T}}\Big)\\ &+\Big(\sum_A t_{TA}R_A\Big)H^{11}\Big[-(3\boldsymbol{\tau}_1\cdot\bar{\mathbf{x}}^m_{,\xi\xi}-g_N\mathbf{n}\cdot\bar{\mathbf{x}}^m_{,\xi\xi\xi})\lfloor\mathbf{D}_1\rfloor_s\lfloor\mathbf{D}_1\rfloor_s^{\mathrm{T}} - \lfloor\mathbf{N}\rfloor_s\lfloor\bar{\mathbf{N}}_1\rfloor_s^{\mathrm{T}}\\ &-\lfloor\bar{\mathbf{N}}_1\rfloor_s\lfloor\mathbf{N}\rfloor_s^{\mathrm{T}} - \frac{1}{m_{11}}(\lfloor\mathbf{T}\rfloor_s\lfloor\bar{\mathbf{T}}_1\rfloor_s^{\mathrm{T}}+\lfloor\bar{\mathbf{T}}_1\rfloor_s\lfloor\mathbf{T}\rfloor_s^{\mathrm{T}}\Big]\,\mathrm{d}\Gamma.\end{aligned} \tag{A.16}$$

The Gauss-quadrature rule can be applied to evaluate the integral in (A.15) and (A.16). The tangent stiffness matrix for the contact problem is simply obtained as

$$\lfloor\mathbf{K}_c\rfloor_s = \lfloor\mathbf{K}_{c,m}\rfloor_s + \lfloor\mathbf{K}_{c,g}\rfloor_s. \tag{A.17}$$

Appendix B Validation of the random field generation method

To validate the random field generation method, especially its capacity in preserving the prescribed correlation structure and height distribution, a further investigation is performed by checking the correlation coefficients and the normalised probability density function of the numerical realisations. Specifically, a general form of exponential type correlation function and Matérn type correlation function is studied as

$$\begin{aligned} R_{\exp}(\mathbf{x},\mathbf{x}') &= \mathrm{e}^{-(\frac{\|\mathbf{x}-\mathbf{x}'\|}{l})^n}, \\ R_{\mathrm{mat}}(\mathbf{x},\mathbf{x}') &= \frac{2^{1-\nu}}{\Gamma(\nu)}(\sqrt{2\nu}\frac{\|\mathbf{x}-\mathbf{x}'\|}{l})^{\nu}\ \mathrm{K}_{\nu}(\sqrt{2\nu}\frac{\|\mathbf{x}-\mathbf{x}'\|}{l}). \end{aligned} \tag{B.1}$$

where n , ν are manually defined parameters, $\Gamma(z) = \int_0^{\infty} \mathrm{e}^{-t}t^{z-1}\mathrm{d}t$ is the gamma function and $\mathrm{K}_{\nu}(\bullet)$ is the modified Bessel function. The 1D random field generated in Sec.2.2.4 is reinvestigated here by applying different correlation structures as shown in (B.1) with parameters $n = \{1.5, 2.0\}$ and $\nu = \{0.5, 10\}$. The correlation coefficient is defined as

$$\rho(x_1, x_2) = \frac{\mathbb{E}[(x_1 - \mu_{x_1})(x_2 - \mu_{x_2})]}{\sigma_{x_1}\sigma_{x_2}}, \tag{B.2}$$

where $\mu_x = \mathbb{E}(x)$ and $\sigma_x = \mathbb{E}[(x - \mu_x)^2]$ is calculated from the numerical realisations of each case and compared with the theoretical result shown in Fig.B.1. It can be observed that the current random field generation method can preserve well the prescribed correlation structure. Moreover, the probability density function of height distributions are computed and compared with the theoretical Gaussian distribution results, as shown in Fig.B.2, which shows their consistency.

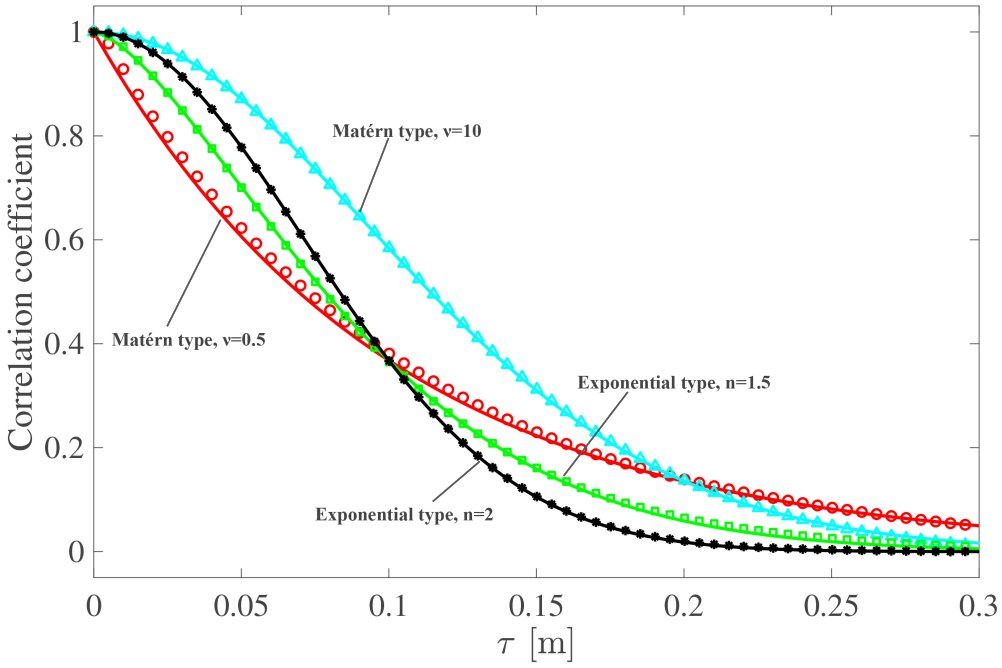

Fig. B.1. Correlation structure validation. Solid line - theoretical results; dot - numerical results.

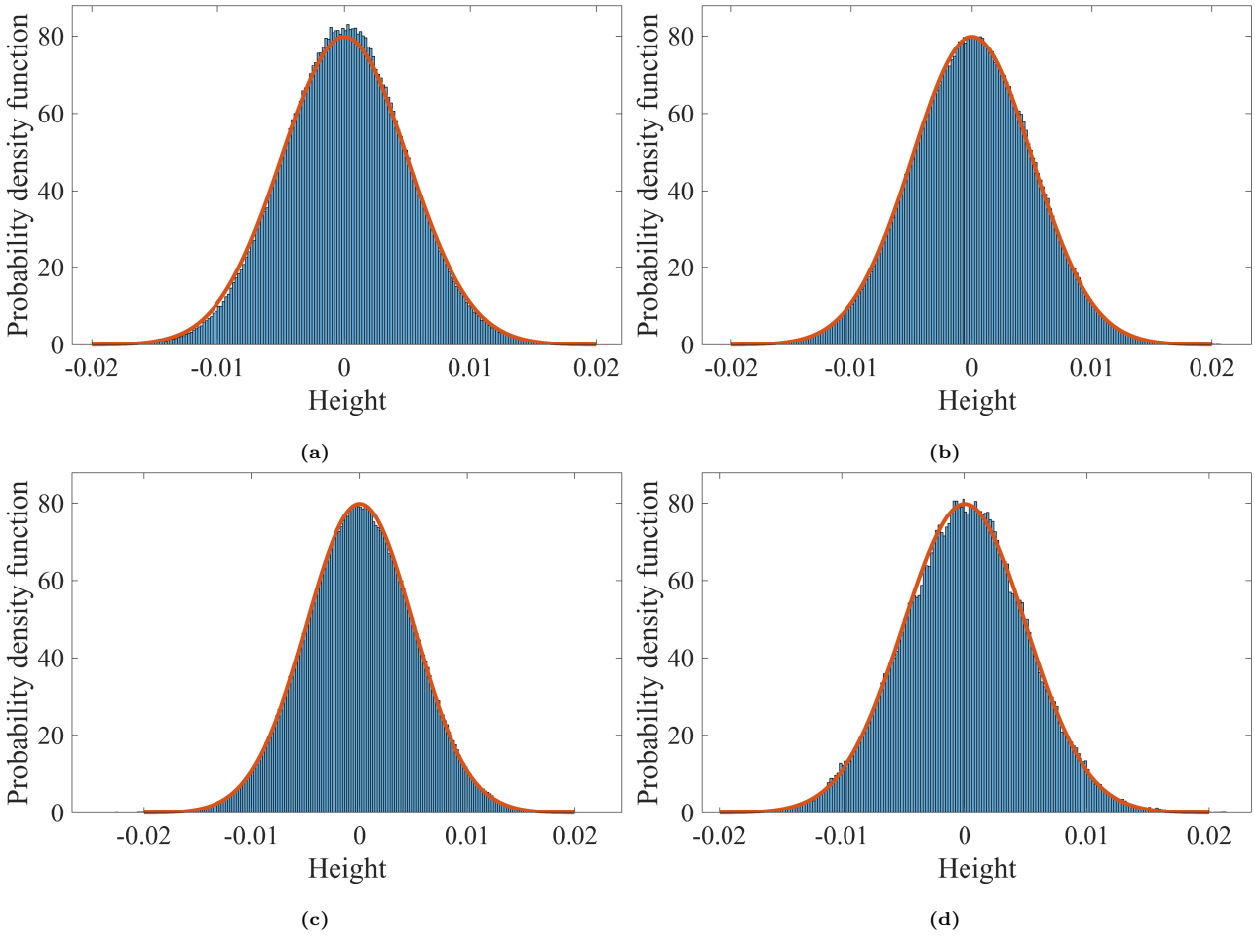

Fig. B.2. Height distribution with correlation structure (a) exponential type, $n = 1.5$; (b) exponential type, $n = 2$; (c) matérn type, $\nu = 0.5$; (d) matérn type, $\nu = 10.0$. Solid line - analytical function, bars - numerical realisations.

References

[1] J. A. Greenwood, J. P. Williamson, Contact of nominally flat surfaces, Proceedings of the royal society of London. Series A. Mathematical and physical sciences 295 (1442) (1966) 300–319.

[2] S. Kucharski, G. Starzyński, Contact of rough surfaces under normal and tangential loading, Wear 440 (2019) 203075.

[3] D. J. Whitehouse, J. Archard, The properties of random surfaces of significance in their contact, Proceedings of the Royal Society of London. A. Mathematical and Physical Sciences 316 (1524) (1970) 97–121.

[4] B. Persson, Elastoplastic contact between randomly rough surfaces, Physical Review Letters 87 (11) (2001) 116101.

[5] B. N. Persson, O. Albohr, U. Tartaglino, A. Volokitin, E. Tosatti, On the nature of surface roughness with application to contact mechanics, sealing, rubber friction and adhesion, Journal of physics: Condensed matter 17 (1) (2004) R1.

[6] P. Wriggers, Computational contact mechanics, Computational Mechanics 32 (1-2) (2003) 141–141.

[7] T. A. Laursen, Computational contact and impact mechanics: fundamentals of modeling interfacial phenomena in nonlinear finite element analysis, Springer Science & Business Media, 2013.

[8] G. Zavarise, L. De Lorenzis, The node-to-segment algorithm for 2d frictionless contact: classical formulation and special cases, Computer Methods in Applied Mechanics and Engineering 198 (41-44) (2009) 3428–3451.

[9] G. Zavarise, P. Wriggers, A segment-to-segment contact strategy, Mathematical and Computer Modelling 28 (4-8) (1998) 497–515.

[10] T. McDevitt, T. Laursen, A mortar-finite element formulation for frictional contact problems, International Journal for Numerical Methods in Engineering 48 (10) (2000) 1525–1547.

[11] L. De Lorenzis, P. Wriggers, C. Weißenfels, Computational contact mechanics with the finite element method, Encyclopedia of computational mechanics second edition (2017) 1–45.

[12] R. Pohrt, Q. Li, Complete boundary element formulation for normal and tangential contact problems, Physical Mesomechanics 17 (4) (2014) 334–340.

[13] W. W. Chen, S. Liu, Q. J. Wang, Fast Fourier transform based numerical methods for elasto-plastic contacts of nominally flat surfaces, Journal of Applied Mechanics 75 (1) (2008).

[14] T. J. Hughes, J. A. Cottrell, Y. Bazilevs, Isogeometric analysis: CAD, finite elements, NURBS, exact geometry and mesh refinement, Computer methods in applied mechanics and engineering 194 (39-41) (2005) 4135–4195.

[15] R. A. Sauer, Local finite element enrichment strategies for 2D contact computations and a corresponding post-processing scheme, Computational Mechanics 52 (2) (2013) 301–319.

[16] R. A. Sauer, Enriched contact finite elements for stable peeling computations, International Journal for numerical methods in engineering 87 (6) (2011) 593–616.

[17] B. Yang, T. A. Laursen, X. Meng, Two dimensional mortar contact methods for large deformation frictional sliding, International journal for numerical methods in engineering 62 (9) (2005) 1183–1225.

[18] A. Popp, M. W. Gee, W. A. Wall, A finite deformation mortar contact formulation using a primal-dual active set strategy, International Journal for Numerical Methods in Engineering 79 (11) (2009) 1354–1391.

[19] I. Temizer, P. Wriggers, T. Hughes, Contact treatment in isogeometric analysis with NURBS, Computer Methods in Applied Mechanics and Engineering 200 (9-12) (2011) 1100–1112.

[20] L. De Lorenzis, I. Temizer, P. Wriggers, G. Zavarise, A large deformation frictional contact formulation using NURBS-based isogeometric analysis, International Journal for Numerical Methods in Engineering 87 (13) (2011) 1278–1300.

[21] J. Lu, Isogeometric contact analysis: Geometric basis and formulation for frictionless contact, Computer Methods in Applied Mechanics and Engineering 200 (5-8) (2011) 726–741.

[22] J.-Y. Kim, S.-K. Youn, Isogeometric contact analysis using mortar method, International Journal for Numerical Methods in Engineering 89 (12) (2012) 1559–1581.

[23] L. De Lorenzis, P. Wriggers, T. J. Hughes, Isogeometric contact: a review, GAMM-Mitteilungen 37 (1) (2014) 85–123.

[24] I. Temizer, P. Wriggers, T. Hughes, Three-dimensional mortar-based frictional contact treatment in isogeometric analysis with NURBS, Computer Methods in Applied Mechanics and Engineering 209 (2012) 115–128.

[25] L. De Lorenzis, P. Wriggers, G. Zavarise, A mortar formulation for 3D large deformation contact using NURBS-based isogeometric analysis and the augmented Lagrangian method, Computational Mechanics 49 (1) (2012) 1–20.

[26] M. Matzen, T. Cichosz, M. Bischoff, A point to segment contact formulation for isogeometric, NURBS based finite elements, Computer Methods in Applied Mechanics and Engineering 255 (2013) 27–39.

[27] M. Matzen, M. Bischoff, A weighted point-based formulation for isogeometric contact, Computer Methods in Applied Mechanics and Engineering 308 (2016) 73–95.

[28] R. A. Sauer, L. De Lorenzis, An unbiased computational contact formulation for 3D friction, International Journal for Numerical Methods in Engineering 101 (4) (2015) 251–280.

[29] R. A. Sauer, L. De Lorenzis, A computational contact formulation based on surface potentials, Computer Methods in Applied Mechanics and Engineering 253 (2013) 369–395.

[30] T. X. Duong, L. De Lorenzis, R. A. Sauer, A segmentation-free isogeometric extended mortar contact method, Computational Mechanics 63 (2) (2019) 383–407.

[31] V. Agrawal, S. S. Gautam, Varying-order NURBS discretization: An accurate and efficient method for isogeometric analysis of large deformation contact problems, Computer Methods in Applied Mechanics and Engineering 367 (2020) 113125.

[32] L. De Lorenzis, J. Evans, T. J. Hughes, A. Reali, Isogeometric collocation: Neumann boundary conditions and contact, Computer Methods in Applied Mechanics and Engineering 284 (2015) 21–54.

[33] R. Kruse, N. Nguyen-Thanh, L. De Lorenzis, T. J. Hughes, Isogeometric collocation for large deformation elasticity and frictional contact problems, Computer Methods in Applied Mechanics and Engineering 296 (2015) 73–112.

[34] I. Temizer, Computational homogenization of soft matter friction: Isogeometric framework and elastic boundary layers, International Journal for Numerical Methods in Engineering 100 (13) (2014) 953–981.

[35] K. Kılıç, I. Temizer, Tuning macroscopic sliding friction at soft contact interfaces: interaction of bulk and surface heterogeneities, Tribology International 104 (2016) 83–97.

[36] Y. Tong, M. Müller, G.-P. Ostermeyer, Investigations on the dynamic influence of the contact angle on frictional sliding processes between rough surfaces using NURBS and mortar-based augmented Lagrangian method, Tribology International (2021) 106889.

[37] J. A. Cottrell, T. J. Hughes, Y. Bazilevs, Isogeometric analysis: toward integration of CAD and FEA, John Wiley & Sons, 2009.

[38] L. Piegl, W. Tiller, The NURBS book, Springer Science & Business Media, 1996.

[39] S. Rahman, A Galerkin isogeometric method for Karhunen-Loève approximation of random fields, Computer Methods in Applied Mechanics and Engineering 338 (2018) 533–561.

[40] R. Jahanbin, S. Rahman, An isogeometric collocation method for efficient random field discretization, International Journal for Numerical Methods in Engineering 117 (3) (2019) 344–369.

[41] R. G. Ghanem, P. D. Spanos, Stochastic finite elements: a spectral approach, Courier Corporation, 2003.

[42] W. Betz, I. Papaioannou, D. Straub, Numerical methods for the discretization of random fields by means of the Karhunen-Loève expansion, Computer Methods in Applied Mechanics and Engineering 271 (2014) 109–129.

[43] F. Auricchio, L. B. Da Veiga, T. Hughes, A. Reali, G. Sangalli, Isogeometric collocation methods, Mathematical Models and Methods in Applied Sciences 20 (11) (2010) 2075–2107.

[44] J. Jang, K. Kim, Modeling of a microscale surface using NURBS technique, Coatings 9 (12) (2019) 775.

[45] P. S. Lockyer, Controlling the interpolation of NURBS curves and surfaces, Ph.D. thesis, University of Birmingham (2007).

[46] T. Zohdi, Constrained inverse formulations in random material design, Computer Methods in Applied Mechanics and Engineering 192 (28-30) (2003) 3179–3194.

[47] Q. Feng, A discrete model of a stochastic friction system, Computer Methods in Applied Mechanics and Engineering 192 (2003) 2339–2354.

[48] H. Hu, A. Batou, H. Ouyang, Coefficient of friction random field modelling and analysis in planar sliding, Journal of Sound and Vibration 508 (2021) 116197.

[49] M. Cocu, E. Pratt, M. Raous, Formulation and approximation of quasistatic frictional contact, International Journal of Engineering Science 34 (7) (1996) 783–798.

[50] P. Farah, A. Popp, W. A. Wall, Segment-based vs. element-based integration for mortar methods in computational contact mechanics, Computational Mechanics 55 (1) (2015) 209–228.

[51] N. Kikuchi, J. T. Oden, Contact problems in elasticity: a study of variational inequalities and finite element methods, SIAM, 1988.

[52] M. Stembalski, P. Preś, W. Skoczyński, Determination of the friction coefficient as a function of sliding speed and normal pressure for steel C45 and steel 40HM, Archives of civil and mechanical engineering 13 (4) (2013) 444–448.